

Article

Late Paleozoic–Early Mesozoic Granite Magmatism on the Arctic Margin of the Siberian Craton during the Kara-Siberia Oblique Collision and Plume Events

Valery A. Vernikovsky ^{1,2,*} , Antonina Vernikovskaya ^{1,2}, Vasilij Proskurnin ³, Nikolay Matushkin ^{1,2} , Maria Proskurnina ³, Pavel Kadilnikov ¹, Alexander Larionov ³ and Alexey Travin ⁴

¹ A.A. Trofimuk Institute of Petroleum Geology and Geophysics, Siberian Branch of the Russian Academy of Sciences, 630090 Novosibirsk, Russia; vernikovskayaae@ipgg.sbras.ru (A.V.); matushkinny@ipgg.sbras.ru (N.M.); kadilnikovpi@ipgg.sbras.ru (P.K.)

² Department of Geology and Geophysics, Novosibirsk State University, 630090 Novosibirsk, Russia

³ A.P. Karpinsky Russian Geological Research Institute, 199106 St. Petersburg, Russia; vasily_proskurnin@vsegei.ru (V.P.); maria_proskurnina@vsegei.ru (M.P.); Alexander_Larionov@vsegei.ru (A.L.)

⁴ V.S. Sobolev Institute of Geology and Mineralogy, Siberian Branch of the Russian Academy of Sciences, 630090 Novosibirsk, Russia; travin@igm.nsc.ru

* Correspondence: VernikovskyVA@ipgg.sbras.ru; Tel.: +7-383-363-40-16

Received: 29 May 2020; Accepted: 24 June 2020; Published: 25 June 2020



Abstract: We present new structural, petrographic, geochemical and geochronological data for the late Paleozoic–early Mesozoic granites and associated igneous rocks of the Taimyr Peninsula. It is demonstrated that large volumes of granites were formed due to the oblique collision of the Kara microcontinent and the Siberian paleocontinent. Based on U-Th-Pb isotope data for zircons, we identify syncollisional (315–282 Ma) and postcollisional (264–248 Ma) varieties, which differ not only in age but also in petrochemical and geochemical features. It is also shown that as the postcollisional magmatism was coming to an end, Siberian plume magmatism manifested in the Kara orogen and was represented by basalts and dolerites of the trap formation (251–249 Ma), but also by differentiated and individual intrusions of monzonites, quartz monzonites and syenites (Early–Middle Triassic) with a mixed crustal-mantle source. We present a geodynamic model for the formation of the Kara orogen and discuss the relationship between collisional and trap magmatism.

Keywords: granites; petrography; geochemistry; U-Th-Pb and ⁴⁰Ar/³⁹Ar geochronology; carboniferous; Permian; Triassic; Siberian Craton; Kara microcontinent; oblique collision; Kara orogen; Siberian plume

1. Introduction

The Taimyr-Severnaya Zemlya fold-and-thrust area is one of the key structures of the Arctic (Figure 1) that has been attracting the attention of researchers with its complex geology, remoteness of access, and mineral resources (e.g., [1–15]). The evolution of this domain can be traced from at least the Meso–Neoproterozoic, allowing comparison to other key Arctic structures and their development, as well as enabling us to develop paleogeodynamic reconstructions for the Arctic Ocean (e.g., [13,15–31]).

There are several different models for the formation of the Taimyr-Severnaya Zemlya fold-and-thrust area and we will discuss these within the context of our new data. Having worked in this region for several decades, we identify two main periods of development. The first is a late

Precambrian stage corresponding to the formation in the Neoproterozoic, and subsequent accretion in the Ediacaran, of the Central Taimyr belt to the Siberian paleocontinent. The second is a late Paleozoic–Early Triassic stage, during which the Kara microcontinent collided with Siberia, leading to the formation of the Kara (Taimyr-Severnaya Zemlya) orogen, closely followed by the trap magmatism related to the Siberian plume [13,32–35].

In this study, the main focus is given to the second, late Paleozoic–early Mesozoic stage, during which collision resulted in the formation of large volumes of granitoids of various types. Their geological position, petro-geochemical compositions and ages enable us to decipher the tectonic structure of the whole orogenic belt and its formation mechanism. Furthermore, in this paper we discuss manifestations of the main phase (251–249 Ma) of the Siberian plume trap magmatism in the Kara orogen [34,36–45] and its relationships to the syncollisional and postcollisional granitoids.

The Taimyr granites were extensively studied in the 1950–1970s. For example, M.G. Ravich and L.A. Chayka not only studied the metamorphic and igneous rocks of Taimyr, but also described for the first time the “small intrusions of the Byrranga Ridge” and identified the differentiated intrusions as part of the Siberian traps [46–48]. Without any isotope-geochronological data, these researchers considered that most of the metamorphic and igneous rocks of Taimyr were Precambrian in age. In those years, this opinion was widely held, probably due to the widespread occurrence of autochthonous granites in Northern and Central Taimyr that had formed in-situ and were metamorphosed into gneisses of the amphibolite facies. A.M. Daminova had a different opinion based on the geological data and considered that the two-mica Taimyr granites were of Hercynian age, or, more precisely—Carboniferous-Permian [4]. Nonetheless, L.V. Makhlaev and N.I. Korobova considered the Taimyr granites as Precambrian and defined the “genetic granitoid series of the Precambrian of Taimyr” [49], that is to say, granites that formed by the re-melting of various crustal materials—carbonaceous-greywacke, greywacke, pelitic or basic. At the same time, in addition to the autochthonous granites, they described parautochthonous and allochthonous granites. The former they described as “located in direct proximity from the zone of ultrametamorphism and granite-formation”, but “intruding into the overlying metamorphic rocks of epidote-amphibolite and greenschist facies”. The latter are clearly discordant bodies with intrusive contacts and, commonly, with contact hornfelsed rims.

Further studies of the Taimyr granites using precise isotope-geochronological methods established that their ages are Paleozoic—from 315 to 250 Ma [32,50–53] and also identified late Carboniferous (autochthonous) and early Permian (parautochthonous) syncollisional granitoids, as well as late Permian postcollisional (allochthonous) granitoids with compositions ranging from S-type granites to transitional S-I- and A-types [54,55].

Additionally, previous workers noted that the formation of the Kara orogen was the result of oblique collision, which is indicated by geological data, namely the orientations of the main structural elements of the orogen that correspond with the strike of the largest dextral strike-slip fault zones [7,13], and by paleomagnetic data [20,31,35]. The granitoids have a good correlation with the structures of the Kara orogen—the syncollisional (autochthonous and parautochthonous) ones are located in the western and central part, and the postcollisional (allochthonous) ones in the eastern part.

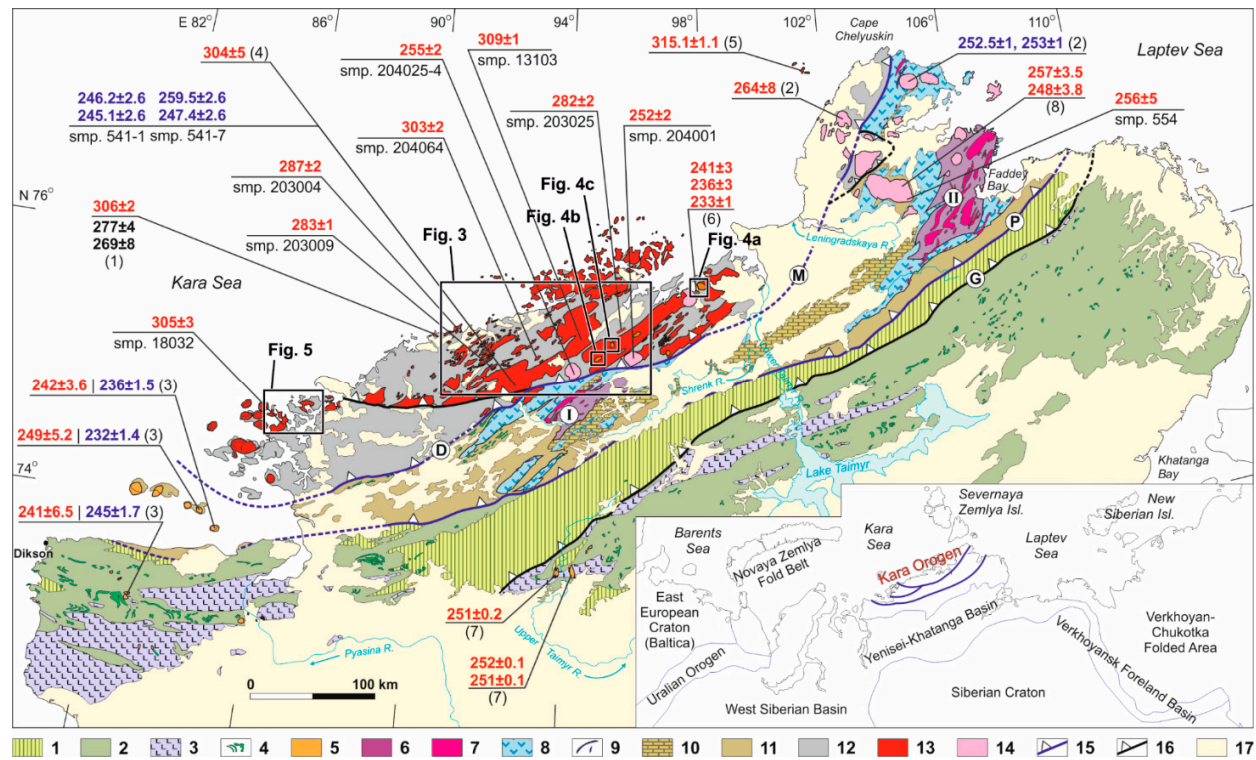


Figure 1. Tectonic map of the Taimyr Peninsula part of the Kara orogen simplified from [10] with tectonic zoning from [12,13,17]. 1–2—Southern Domain—South Taimyr fold belt (deformed passive continental margin of Siberia): 1—mainly dolomites and limestones (O–C₂); 2—mainly sandstones, mudstones, coal bearing deposits (C₃–P₂); 3–5—deformed Siberian trap formations (P₃–T₁): 3—basalts and tuffs; 4—dolerite sills; 5—alkaline syenites, granites, monzonites; 6–11—Central Domain—Central Taimyr accretionary belt: 6—Mamont-Shrenk (I) and Faddey (II) cratonic terranes; 7—Neoproterozoic granitoids (940–850 Ma); 8— island arc complexes (NP₁); 9—ophiolites, including plagiogranites (750–730 Ma); 10—carbonate rocks terranes; 11—sedimentary cover (NP₃–C₁); 12—Northern Domain—deformed and reworked rocks of the passive continental margin of the Kara microcontinent: rhythmically alternating metasandstones, metasiltstones, metapelites, carbonaceous shales (NP₃–C); 13—syncollisional granites; 14—postcollisional granites; 15—sutures: M—Main Taimyr, P—Pyasina-Faddey, D—Diabasoviy; 16—thrusts (G—Pogranichniy); 17—Jurassic–Quaternary deposits including the Yenisei-Khatanga basin. Colored numbers show ages for granitoids (Ma): red—U–Pb for zircons, blue—Ar/Ar method, black—Rb–Sr method. Under the ages are given sample numbers from this study. Reference sources in brackets: (1)—[50], (2)—[13], (3)—[34], (4)—[51], (5)—[52], (6)—[56]; (7)—[45]; (8)—[53].

Thus, the Kara orogen can be considered an example of the most common type of oblique collision, when the orientation of the main strain deviates from the perpendicular to the convergent margin [57]. This is reflected in the spatial distribution of thermal fields within the orogen and in changes in age characteristics of granites and metamorphic rocks in the complexes. At the same time, the duration of collisional events can be in the tens of millions of years [15,57–60]. According to S.P. Korikovsky, the collisional stacking and thickening of the crust leads to progressive regional zonal metamorphism and terminates as a final stage of ultrametamorphism and anatexis leading to anatectic granitoids and autochthonous-type migmatites [58]. Korikovsky estimated that the interval between the early zonal metamorphism and the subsequent orogenic magmatism is 5 to 20 m.y. According to other estimates [61], syn-kinematic migmatites form 15–20 m.y. after the start of the collision.

The new data obtained in recent years have significantly broadened our ideas on the duration of collisional magmatism and of the syn- and postcollisional stages between the Kara microcontinent and the Siberian craton. They also allow us to discuss the effect of the Permian-Triassic plume event on the final stage of formation of the Kara orogen.

2. Tectonic Setting

The Taimyr-Severnaya Zemlya orogen is a late Paleozoic–early Mesozoic, NE-striking fold-and-thrust belt [10,12,13,17,32] that can be traced for almost 1000 km along the Kara Sea coast (Figure 1). It is situated between the Ural-Novaya Zemlya orogen in the west and the Verkhoyansk fold belt in the east. Its southern boundary is buried under the Mesozoic and Cenozoic sediments of the Yenisey-Khatanga basin, and its northern part is exposed in the Severnaya Zemlya archipelago [7,14]. This fold-and-thrust belt is divided into three NE-trending tectonostratigraphic domains (Southern, Central, and Northern). The three domains are connected by sutures with thrust kinematics (Figure 1)—the Pyasina-Faddey, Main Taimyr, and Diabasoviy sutures [2,10,12,13,62].

The Southern Domain corresponds to the deformed northwestern passive margin of the Siberian Craton. It is composed of an unmetamorphosed Ordovician–Permian shallow marine platform (carbonate-dominated) succession covered by late Permian–Early Triassic sandstones, and hosting flood basalts and dolerite sills of the Siberian traps [10,12,14,63]. All rocks of the Southern Domain are folded and thrust southward, with a significant decrease in the intensity of both folding and faulting to the south. The domain also contains numerous alkaline (ultra)basic to felsic magmatic complexes in the form of layered intrusions, sills and dikes. Some of these differentiated intrusions, dolerite sills and small syenite plutons have been dated between 251 and 241 Ma (U-Pb data on zircons) [34,43,45,64].

The Central Domain is an accretionary belt [33] and is mainly composed of Neoproterozoic sedimentary and volcanic rocks, including ophiolites and island arc magmatic suites, and segments of continental crust [12,54,65–68]. The accretion of the belt to the Siberian paleocontinent took place in the Ediacaran (606–570 Ma), which has been established from geological data and from Sm-Nd and Rb-Sr ages of metamorphism of the protolith of garnet amphibolites in the junction zone between the Central and Southern Taimyr domains [69]. The tectonic contacts along thrust faults between individual blocks and sheets are commonly marked by cataclastic, mylonitic, and autoclastic mélangé zones. These Precambrian rocks were folded and thrust together in the latest Neoproterozoic and were covered by Ediacaran–Paleozoic successions [10–13].

Taimyr's Northern Domain corresponds to the deformed southern margin of the Kara microcontinent. It is composed of a Neoproterozoic–Cambrian succession dominated by turbidites, which were described in detail as a flyschoid series [8]. Later, these rhythmically alternating sandstones, siltstones and shales have been interpreted as continental slope and rise sediments [12,13,17]. Blocks of amphibolites and biotite-amphibolite crystalline schists are present but are less widespread. They have tectonic contacts with the flyschoid deposits and are probably blocks of the Central Taimyr accretionary belt exposed in erosional and tectonic windows. This is corroborated by comparisons of the chemical composition of these amphibolites and biotite-amphibole crystalline schists with compositions of meta-andesite-basalts of the Central Domain accretionary belt [13].

The zoned regional metamorphism of these deposits from the greenschists to amphibolite facies, with the formation of zones of sub-stratigraphic migmatization and granitization, complicate the structure of this domain [4,8,13,49,70–74]. The Precambrian complexes composing the basement of the Kara microcontinent are raised above sea level both in the northern part of the Taimyr Peninsula and on the Severnaya Zemlya archipelago [7,14,15,75,76]. The main structural elements of the southern part of the microcontinent are oriented conformably to the strike of the largest dextral strike-slip fault zones bordering it, which points to the important role of strike-slip tectonics during the formation of the Kara orogen (Figure 2). The Neoproterozoic–Cambrian flysch-like deposits of Severnaya Zemlya are unconformably overlain by Ordovician and Silurian strata of shallow-water, lagoonal, and coastal-marine facies and Devonian Old Red Sandstones [25,75,77–79].

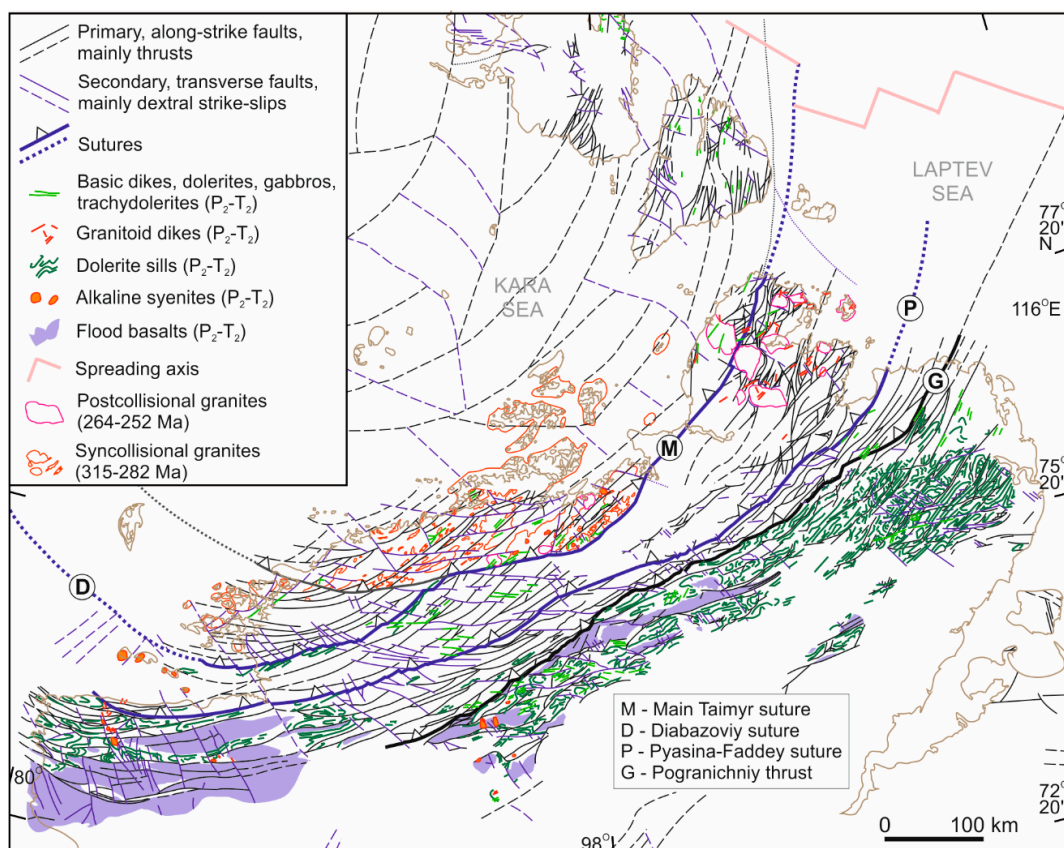


Figure 2. Schematic map of the Kara orogen based on State geological maps (scale 1:1,000,000) [80–83] showing the location patterns of faults and Permian postcollisional and Permian–Triassic Siberian LIP igneous rocks.

Thus, two domains (Southern and Northern) represent the passive margins of two paleocontinents. The sediments of Southern Taimyr correspond to the passive margin of the Siberian continent, whereas the Northern domain represents allochthonous continental slope and rise deposits of the Kara microcontinent. The Central Taimyr accretionary belt lies between them.

The formation of the Kara orogen per se began in the Carboniferous, due to the collision between the Kara microcontinent and the Siberian paleocontinent. We can assess the time of its formation from manifestations of regional metamorphism and granitoid magmatism (315–260 Ma) [50–52,69], and from dislocations along thrusts and strike-slip faults of various scales [7,12–14,20,35].

3. Geology of the Granites

Late Paleozoic granites and regionally metamorphosed rocks can be traced from the southwest to the northeast along the northern part of the Taimyr Peninsula for 700 km. Significant areas are occupied by syncollisional granites located in migmatization zones among rocks of the amphibolite facies, especially in the central part of the Northern Domain (Figure 3). They form intrusions of irregular shape and of various sizes—from lens-like bodies of tens of meters among migmatites to large (several hundred km²) plutons, commonly elongated and concurrent with folds and strike-slip-thrusts (Figures 1 and 3). These bodies can correspond to the parautochthonous varieties described in [49], that is to say, granites that were moved into overlying rocks of epidote-amphibolite and greenschist metamorphism facies with the formation of contact hornfels rims (Figure 3). There are no syncollisional granites to the south of the Main Taimyr and Diabase strike-slip-thrust sutures, which underlines their exclusive localization in the blocks of the orogen that were exhumed from deep levels to the surface. In contrast, postcollisional granite stocks cut through rocks of the Northern and Central Domain, including unmetamorphosed Paleozoic cover deposits in the Central Taimyr accretionary belt. These plutons have oval and rounded shapes, small sizes from several tens to several hundreds of square kilometers, and are localized mainly in the eastern part of the orogen (Figures 1 and 2).

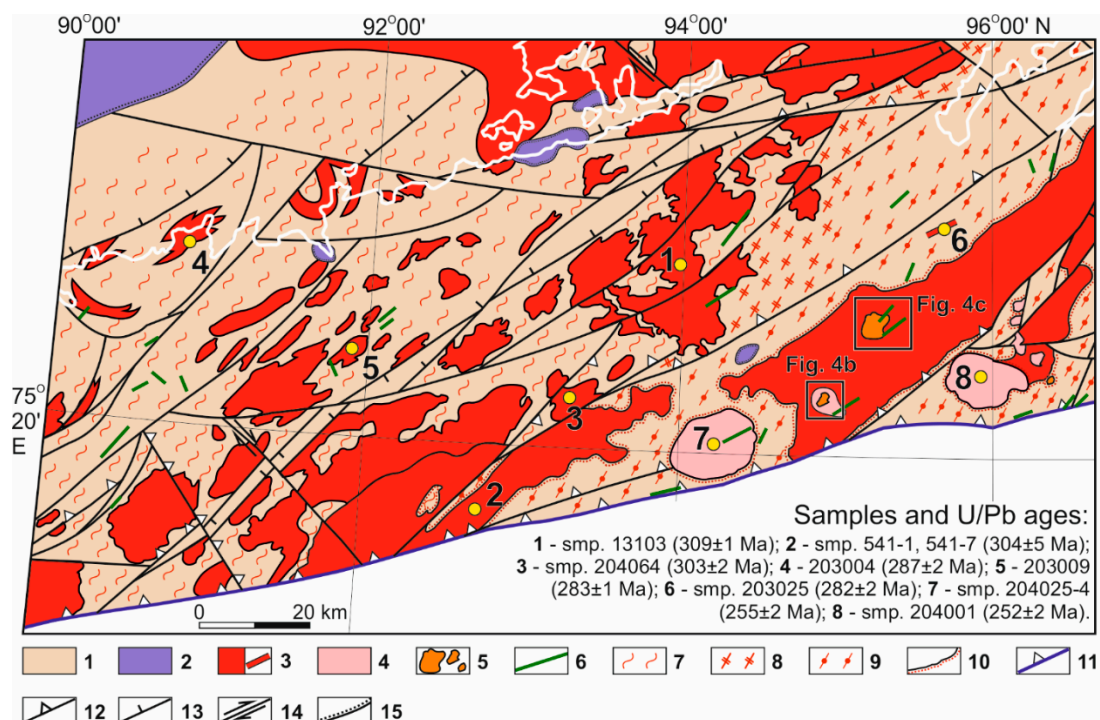


Figure 3. Geology of the central part of the Northern Domain, with locations of some of the studied syn- and postcollisional granitoid intrusions. Modified from state geological map [84]. 1—metasandstones, metasilstones, metapelites, carbonaceous shales (NP₃–C); 2—Jurassic-Cretaceous sands, clays and silts; 3—syncollisional intrusions (315–282 Ma); 4—postcollisional intrusions (264–252 Ma); 5, 6—Siberian LIP intrusions: 5—stocks of alkaline syenites, granites (249–233 Ma), 6—dikes of lamprophyres and gabbro-dolerites; 7–11—metamorphism: 7—amphibolite facies with migmatites; 8—epidote-amphibolite facies; 9—greenschist facies; 10—hornfels rims; 11—Main Taimyr suture; 12—thrusts and reverse faults; 13—normal faults; 14—strike slips; 15—stratigraphic unconformities.

The relationships between syn- and postcollisional granites can often be observed in the field. The type of contact between postcollisional pink biotite-bearing, medium-coarse-grained granite-porphyrines and the coarse-grained, greenish-dark-grey, hornblende-biotite granodiorites was recorded by V.F. Proskurnin in the bed of Oleniy Creek close to Zeeberg Bay (Figure 4).



Figure 4. Field photographs of (a) horizontal weakly-wavy jointing of the postcollisional porphyraceous coarse-grained biotite granites (Oleniy Creek, Zeeberg Bay); (b) contact of pink biotite-bearing medium- to coarse-grained granite-porphyry and greenish-dark-grey hornblende-biotite coarse-grained granodiorites, with apophyses of fine-grained granite-porphyry and aplites in the upper part of the photo accompanying potassium feldspar porphyroblasts in the host granodiorites.

In the region of the Tessema River mouth (western part of Cape Chelyuskin, Northern Domain), the syncollisional two-mica granites intruding metamorphosed flyschoid deposits are themselves cut by a stock of Permian postcollisional hornblende-biotite granite. Here, both granites are also cut by Early Triassic dolerite dikes [85].

Where the postcollisional plutons intrude weakly metamorphosed or unmetamorphosed rocks, these discordant bodies are surrounded by contact metamorphic rims (of the muscovite-hornfels to amphibole-hornfels facies, often with cordierite and andalusite) that are tens to hundreds of meters wide and even reaching several kilometers [11,13,73,86]. Xenoliths of hornfelsed terrigenous host rocks have been identified both in syncollisional and postcollisional granites and granodiorites (Figure 5a). Locally, the amount of inclusions of hornfelsed host rocks can be high and they can reach sizes from 10–20 cm for xenoliths to 150–200 m for the blocks [85].

The contact metamorphic rims may have concordant granodiorite and granite apophyses (Figure 5b). These granitoids are characterized by a widely occurring vein phase, represented by dikes of granite-porphyry and aplite, as well as pegmatite and quartz-feldspar veins.

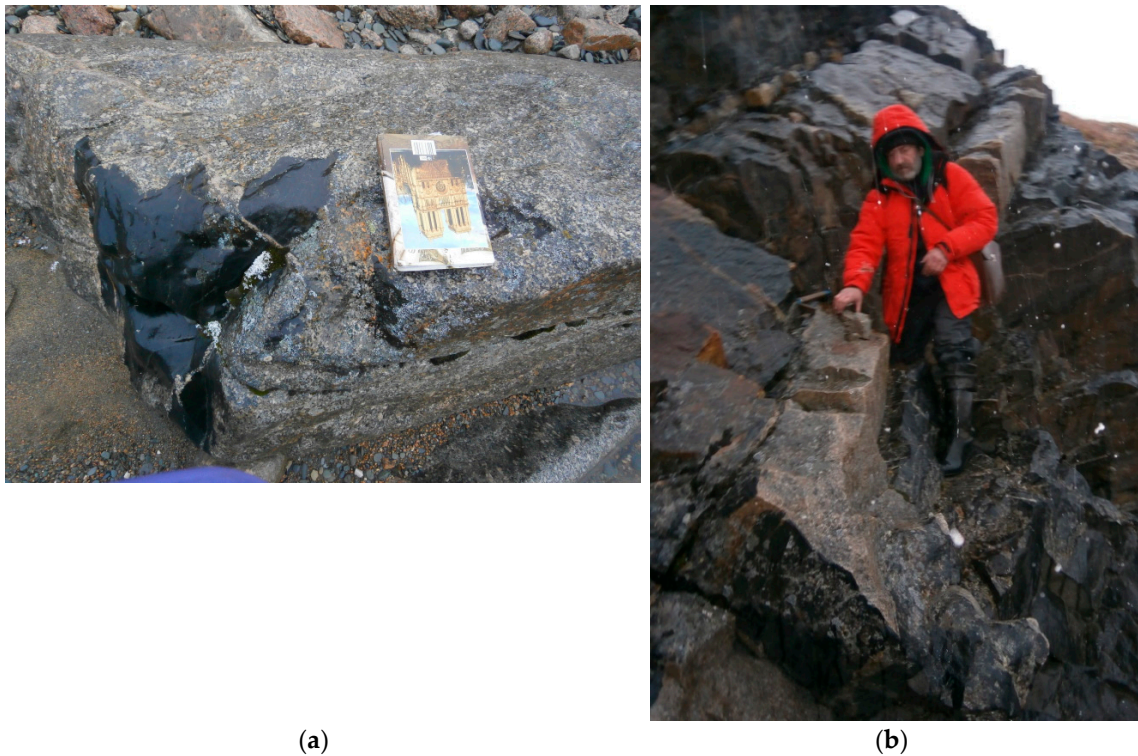


Figure 5. Field photographs of (a) xenoliths of amphibole-hornblende schists in granodiorites in the vicinity of Zeeberg Bay; (b) concordantly occurring granodiorite apophyses in hornfelsed terrigenous host rocks (Oleniy Creek, vicinity of Zeeberg Bay).

Within the Kara orogen, there are also widespread manifestations of traps of the Siberian plume (Figures 1 and 2). Along with basalts, tuffs, and dolerites sills, there are differentiated intrusions, for example the Dumtalei and Dikarabigai ultrabasic to felsic alkaline layered intrusive complexes with compositions ranging from gabbro-dolerites to monzonites and syenites, as well as individual plutons of syenite, monzonite and quartz syenite [34,42,43,45,46,64,87]. These magmatic bodies are most widespread in the Southern Domain, but they also occur in the Central Domain and even the Northern Domain, including the Severnaya Zemlya archipelago (Figures 1–3) [5,6,11,13], which is very important for the determination of the timeline of the main tectonic events. Moreover, these plutons and dikes intrude both Precambrian and Paleozoic formations, including the syncollisional and postcollisional granites. Early–Middle Triassic syenites, monzonites and quartz syenites form small individual intrusions, often cutting the trap basalts and syncollisional granite plutons (Figure 3) [34]. They were also identified within and close to stocks of late Permian postcollisional granitoids, forming ring intrusions, in which the outer borders are represented by late Permian granodiorite or granite, and towards the centers of the intrusions the rocks are transitional to Middle–Late Triassic monzogabbro, monzodiorite, and monzonite to syenite, and quartz syenite (Figure 6) [56].

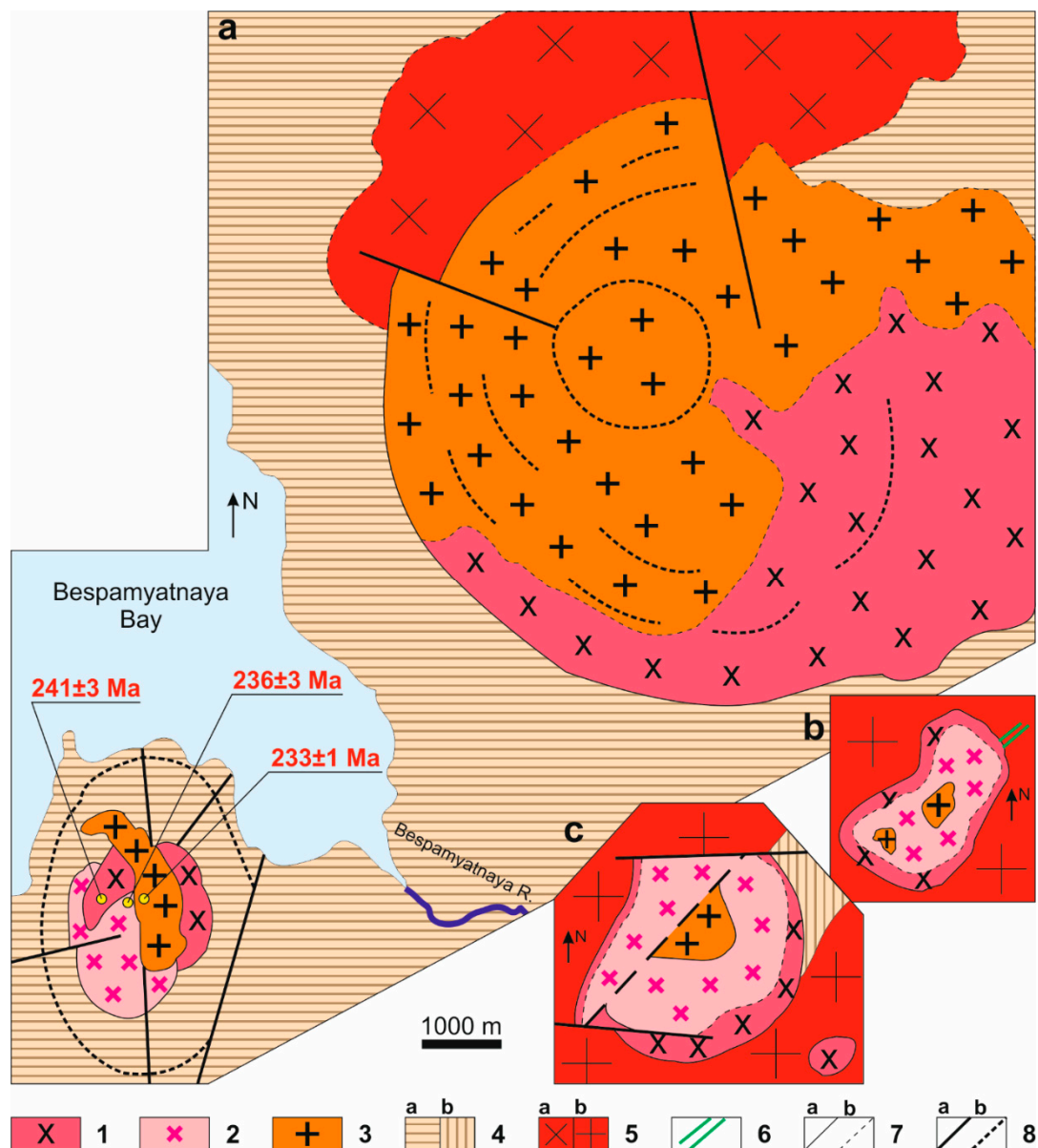


Figure 6. Geological schemes for early Mesozoic ring intrusions in the Northern Domain: (a) in the mouth of Bospamyatnaya River; (b) in the Kamenistaya and Volchya rivers interfluvium; (c) in the upper reaches of Kuropatochya River, modified from [56]. 1–3—Middle–Late Triassic stocks: 1—monzogabbro, monzodiorite, monzonite and monzonite-porphyr (241 ± 3 Ma), 2—syenite, monzonite, syenite-porphyr and syenite-aplite (236 ± 3 Ma), 3—quartz syenite, quartz syenite-porphyr (233 ± 1 Ma); 4—flyschoid terrigenous oligomictic (a) and volcanomictic (b) deposits (NP–Є?); 5—syncollisional granodiorites (a) and granites (b); 6—Early Triassic gabbro-dolerite dikes; 7—determined (a) and inferred (a) geological boundaries; 8—determined (a) and inferred (b) faults. Ages are U–Pb zircon concordia ages from [56]. Panels locations are on Figure 1.

4. Materials—Sampling and Petrography

Samples for petrographic, geochemical and geochronological studies of the granitoids were taken from intrusions of different types in the north and northeast of Taimyr from the Minin Skerries to Cape Chelyuskin (Figure 1). The coordinates and georeferences for studied samples are listed in Appendix A. The syncollisional granitoids, which, after L.V. Makhlaev and N.I. Korobova [49], we assign to the autochthonous and parautochthonous types, form intrusions of irregular shape and of

various sizes—from lens-like bodies of tens of meters among migmatites to large (several hundred km²) plutons, commonly elongated and concurrent with folds and strike-slip-thrusts (Figures 1 and 3). The autochthonous granites are clearly developed in migmatization zones among rocks of the amphibolite facies—migmatized garnet-two-mica sillimanite, garnet-biotite and garnet-hornblende gneisses, where the granites, migmatites and gneisses display gradual transitions. Among these granitoids, granodiorites and porphyroblastic gneissic granites have been identified as well as equigranular “cloud” granites [13,49,88]. These rocks retain relict gneissic banding, skialiths and typically have replacement structures and textures. In contrast, the parautochthonous varieties intrude rocks of the epidote-amphibolite and greenschist facies, usually metasandstones, metasiltsstones and metapelites, forming hornfelsed rims (Figures 3 and 7).

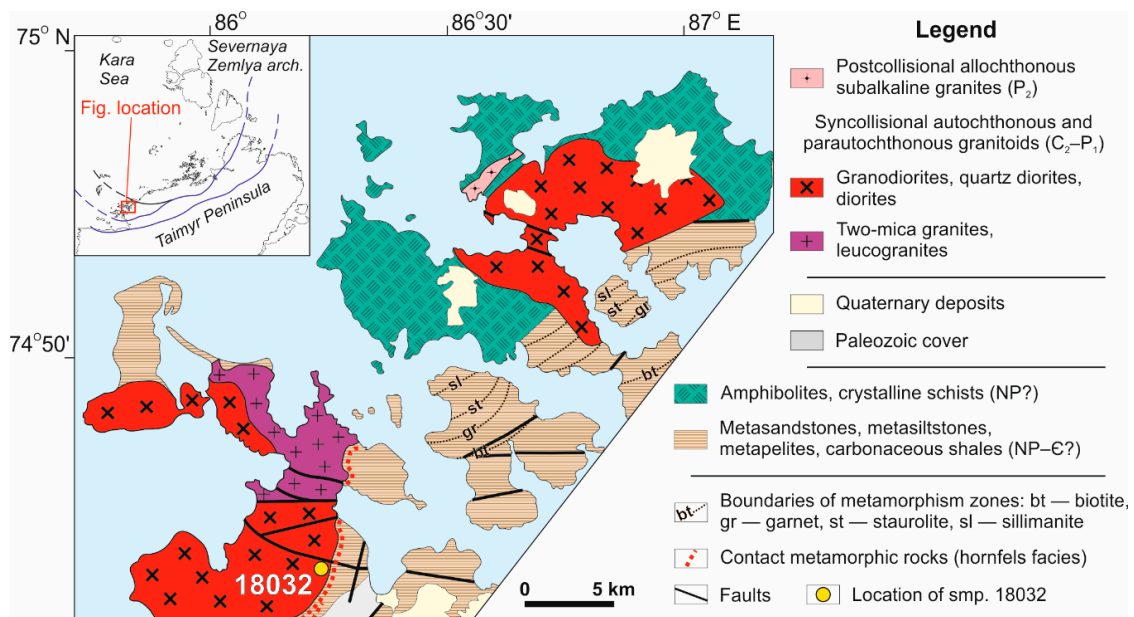


Figure 7. Geological map of part of the region of the Minin Skerries in the western part of the Northern Domain, modified from [84] and the state geological map [81].

The syncollisional granitoids are commonly represented by medium- to coarse-grained granodiorites, sometimes transitioning to quartz diorites and diorites (samples 13103, 204064, 541-1, 541-7, 541-2, 541-4, 543-2) or porphyroblastic biotite-hornblende granodiorite (sample 18032, Minin Skerries). These rocks are mainly (55–60%) composed of large (up to 5 mm) tabular plagioclase porphyroblasts (andesine-oligoclase) among hypidiomorphic to allotriomorphic grains of various sizes (0.2–3 mm) of potassium feldspar (8–10%), quartz (up to 20%), brown biotite (9–12%) and hornblende (3–5%, in diorites approaching the amount of biotite). The rocks are foliated to varying degrees, which is underlined by the subparallel orientation of mica and amphibole grains. Accessory minerals include apatite, titanite, zircon, orthite, rutile, ilmenite, muscovite and sericite.

Syncollisional granitoids also include coarse-grained (up to pegmatoid) porphyroblastic biotite-amphibolite and two-mica granite (samples 203004 and 203009). These granites have a massive, spotted, sometimes gneissic texture. The spotted texture is due to aggregates of rust-red-brown biotite associating with graphite. The porphyroblasts, which can occupy up to 60–70% of the rock volume, are represented by microcline and plagioclase. Tabular feldspar porphyroblasts (up to 5–10 cm long) are commonly subparallel and, together with biotite, form the gneissic foliation. Plagioclase, perthitic potassium feldspar and quartz with undulose extinction are present in close quantities. In addition to these minerals, the groundmass of the rock contains hornblende, muscovite, garnet, titanite and other accessory minerals.

One of the samples was taken from a quartz porphyry dike ~7 m thick (dip angle 70° to 90°) cutting metamorphosed turbidites (Figure 8): folded, thinly interlayering metasiltstones and metasandstones (dip angle 70° to 130°). The quartz porphyry consists of quartz phenocrysts (0.2–1 mm) and a fine-grained quartz-feldspar aggregate. The groundmass has a magnetite impregnation and intense sericitization and chloritization. Accessory minerals include titanite and zircon. Curiously, the petro-geochemical composition and age of the dike rock is close to the coarse-grained porphyroblastic syncollisional granite (samples 203004 and 203009).

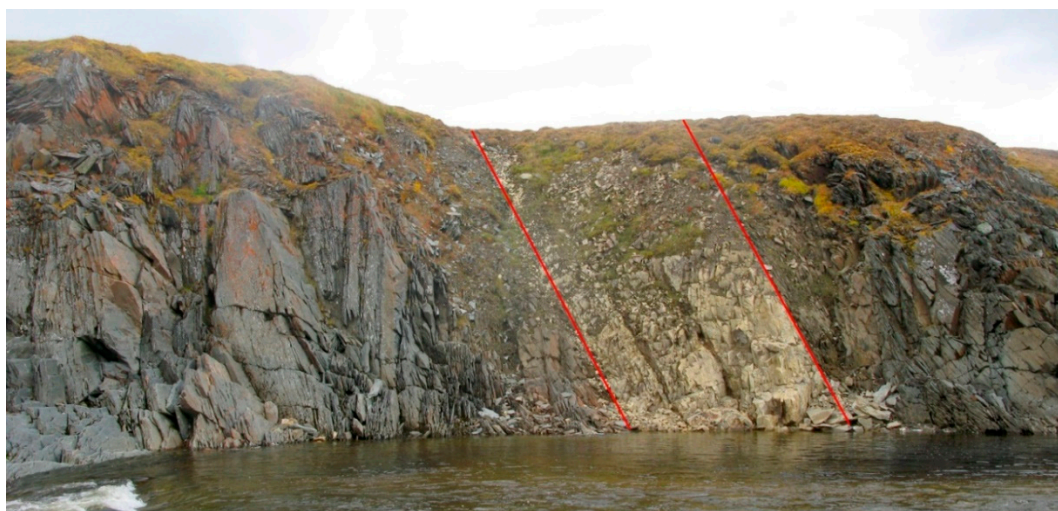


Figure 8. Field photograph of the dike of quartz porphyry (within red lines) cutting thinly interlayering metamorphosed siltstones and sandstones, sample 203025, Spokoynaya R., location on Figure 3.

The postcollisional rocks are represented by allochthonous intrusions of rounded and oval shapes (from 5 × 8 to 20 × 40 km²) of various compositions. They are medium- to coarse-grained porphyreous biotite granite, biotite-amphibole granodiorite, subalkaline granite, granite-porphyry, amphibole-biotite porphyreous, quartz syenite and monzonite (samples 204025/4, 204025/4A, 204001, and 554). Moreover, the marginal parts of the plutons, in their endocontact zones, are composed of quartz diorite and granodiorite, which change into granite towards the central parts of the plutons. These granitoids have a massive, spotted, sometimes gneissic texture and are mostly porphyreous or porphyroblastic. Their mineral composition varies over a wide range: from 5–10% quartz, 45–55% plagioclase, 5–10% potassium feldspar, 20–25% hornblende, and 10–15% biotite in diorite and granodiorite, and up to 25–30% quartz, 30–40% plagioclase, 20–30% potassium feldspar, 0–5% hornblende, and 5–10% biotite in granite and leucogranite. These granitoid plutons are most widespread in the northeastern part of Cape Chelyuskin and in the central part of the orogen (close to the Main Taimyr suture in the region of Zeeberg Bay). There they intrude zonally metamorphosed flyschoid deposits, Carboniferous–Permian syncollisional granite and granodiorite, as well as unmetamorphosed Paleozoic terrigenous-carbonate rocks of the Central Taimyr accretionary belt [11,72,89] (Figures 1 and 3).

5. Analytical Methods

5.1. Major and Trace Element Analyses

The results of X-ray fluorescence and ICP-MS analyses for the studied rocks are given in Appendix B. The analyses were performed at the Central laboratory of A.P. Karpinsky Russian Geological Research Institute (VSEGEI) in Saint Petersburg (Russia) according to their proprietary methodology.

X-ray fluorescence measurements were obtained using an ARL-9800 XRF spectrometer (Thermo Fisher Scientific (Ecuublens) SARL, Switzerland) with an X-ray tube fitted with a Rh anode target disk.

The analyses were undertaken using fused tablets: the analyzed sample was mixed 1:9 with a fusible agent (50% lithium metaborate and 50% lithium tetraborate). The mix was melted in gold-platinum crucibles in a Claisse Fluxer-Bis (Claisse Inc., Canada) fusion instrument. Lower detection limits (wt.%) were: SiO₂—2.0, TiO₂—0.05, Al₂O₃—1.0, Fe₂O₃tot—0.2, MnO—0.01, MgO—0.2, CaO—0.1, Na₂O—0.1, K₂O—0.1, P₂O₅—0.02. Calculations of wt.% of components were done using empirical Lucas-Tooth (multiple regression) constraint equations describing the correspondence between wt.% of a component and its fluorescence intensity. Samples, including calibration standards, were divided into groups according to acidic, basic, and ultrabasic composition.

ICP-MS analyses were performed using two Inductively coupled plasma mass spectrometers: ELAN DRC-e (Perkin Elmer) and Agilent-7700x (Agilent Technologies). The samples were broken down by complete dissolution in a flux of lithium metaborate and by transferring the resulting mix of hard complex oxides in a nitric acid solution. Lower detection limits (ppm) were: Rb—2.0, Sr—1.0, Y—0.1, Zr—0.5, Nb—0.5, Cs—0.1, Ba—3.0, La—0.01, Ce—0.01, Pr—0.01, Nd—0.01, Sm—0.005, Eu—0.005, Gd—0.01, Tb—0.005, Dy—0.01, Ho—0.005, Er—0.01, Tm—0.005, Yb—0.01, Lu—0.005, Hf—0.01, Ta—0.1, Th—0.1, and U—0.1.

5.2. U-Pb SIMS Analytical Technique

The zircons were cast with Buehler EpoKwick resin, along with the Temora [90] and 91500 standards [91]. Then the zircons were half-sectioned and finally polished. Transmitted and reflected light images, as well as BSE and CL images were taken for guidance during analysis.

In-situ U-Pb analyses were performed using the SHRIMP-II SIMS in the Center of Isotopic Research at VSEGEI, applying a secondary electron multiplier in peak-jumping mode following the procedure described in [92]. The analytical data were acquired for nine mass-stations (from ¹⁹⁶Zr₂O to ²⁵⁴UO₂), with four to five mass-spectra per individual analysis. Each fourth to fifth analyses was done on the Temora reference zircons. The results were processed using the software SQUID v1.13 [93] and ISOPLOT/Ex 3.22 [94]. Common lead was corrected using the measured ²⁰⁴Pb/²⁰⁶Pb and the model values of Stacey and Kramers [95]. The results are presented in Appendix C. The ages discussed in the text and error ellipses in the diagrams are at 95% confidence, ratios and corresponding ages in the Table are given with 1σ errors.

5.3. Ar-Ar Dating

Ar-Ar analyses were performed following the procedure described in [96]. The studied monomineral fractions were wrapped in Al foil, placed into quartz ampoules, which were then pumped out and welded. Irradiation was done in the Cd-coated channel of the (BBP-K type) reactor at Tomsk Polytechnic University. Weighted standard samples of monomineral biotite fractions MCA-11 and LP-6 were used as mineral monitors. The gradient of the neutron flux did not exceed 0.5% of the sample size. The experiments using stepwise heating were carried out in a quartz reactor with an external heater. Released Ar was purified using two successive ZrAl SAES getters. The isotopic composition of Ar was measured on a Noble Gas 5400 mass spectrometer (Micromass, UK) in the Analytical Center of IGM SB RAS (Novosibirsk, Russia). The blank for ⁴⁰Ar in the stepwise heating unit was no higher than $n \times 10^{-10}$ ncm³. The results of Ar/Ar measurements and calculations are presented in Appendix D.

6. Results

6.1. Major and Trace Element Geochemistry

The syncollisional intrusive rocks have a wide range of SiO₂ content (60.71–74.66 wt.%), Al₂O₃ (14–18.01 wt.%) and total alkalis (Na₂O + K₂O = 5.25–8.61 wt.%) (Appendix B). They have elevated Na₂O content (2.92–4.81 wt.%) and Na₂O/K₂O ratios in the range 1.06–2.45 (~0.8 in two samples), as well as moderate K₂O contents (2.12–3.93 wt.%). On the TAS diagram, they plot in the fields of diorite,

granodiorite and granite (Figure 9), and on the MALI versus SiO₂ diagram (Figure 10), they correspond to rocks of the calc-alkalic and alkali-calcic magmatic series, with one exception occurring in the calcic series. On the ANK vs ACNK diagram (Figure 11) the granitoids and diorites plot in the peraluminous field with an ACNK index range from 1.04 to 1.55. These samples show similarities in La, Ce, HREE, Hf, Zr, Nb, Ta, Sm, Tb, and Y concentrations with upper and lower continental crust (Figure 12a,b).

The postcollisional intrusive rocks are less diverse in their contents of SiO₂ (66.7–74.5 wt.%) and have high K₂O (4.44–5.33 wt.%) and total alkalis contents (7.99–8.99), moderate Na₂O contents, low Al₂O₃ contents (13.2–15.5 wt.%) and Na₂O/K₂O ratios in the range 0.58–0.83 (Appendix B). On the TAS diagram these samples plot in the fields of granites and quartz monzonites (Figure 9). Most of them correspond to rocks of the alkali-calcic magmatic series, with individual samples extending into the calc-alkalic series (Figure 10). These rocks are weakly peraluminous (ACNK = 1.03–1.08) or weakly metaluminous (ACNK = 0.98) (Figure 11). All postcollisional rocks are depleted in TiO₂ (0.58–0.06 wt.%). These samples demonstrate a similarity in concentrations of REE, Hf, Zr, Nb, Ta, Sm, Tb, and Y with the upper continental crust, although their concentrations of HREE are closely similar to the lower continental crust (Figure 12c,d).

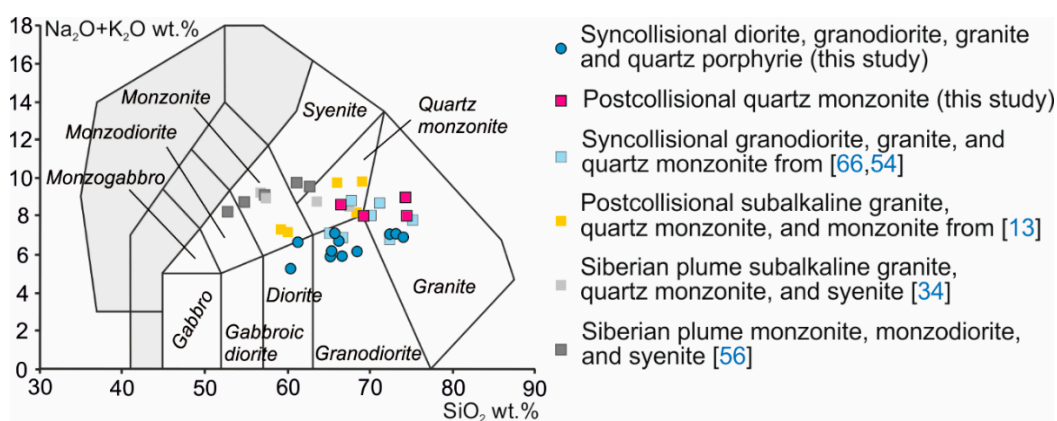


Figure 9. TAS diagram from [97] for the studied felsic rocks.

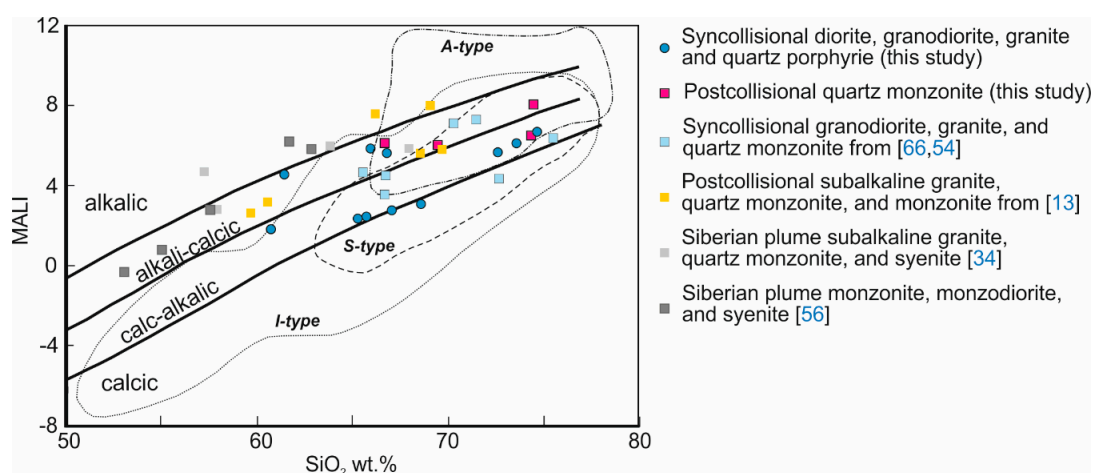


Figure 10. MALI (Na₂O + K₂O - CaO) vs. wt.% SiO₂ diagram after [98] for the studied felsic rocks. Dashed lines show fields of A-type, I-type and S-type granites from the Lachlan Fold Belt [98].

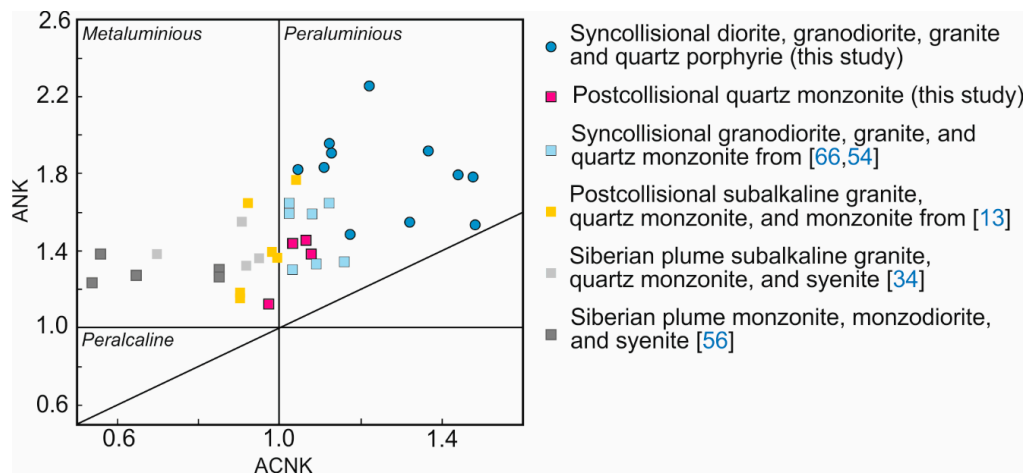


Figure 11. ANK (molar $\text{Al}_2\text{O}_3/(\text{Na}_2\text{O} + \text{K}_2\text{O})$) versus ACNK (molar $\text{Al}_2\text{O}_3/(\text{CaO} + \text{Na}_2\text{O} + \text{K}_2\text{O})$) diagram after [99] for the studied felsic rocks.

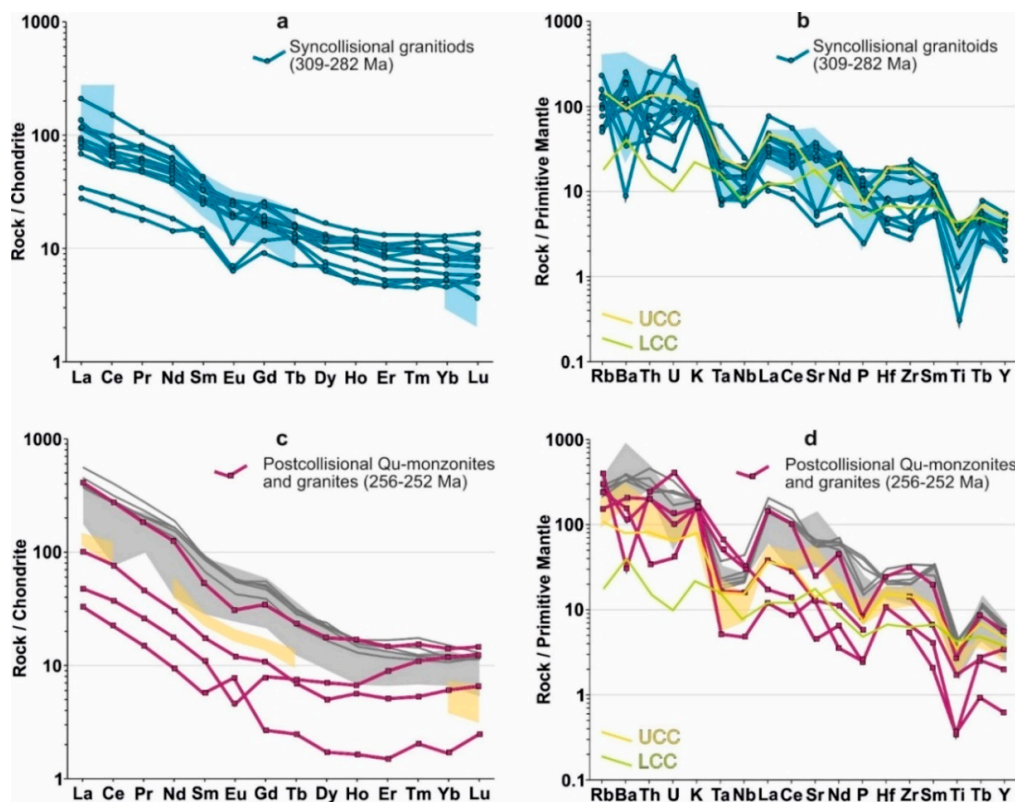


Figure 12. Chondrite-normalized REE distributions (a,c) and primitive mantle-normalized trace elements distributions (b,d) for the studied felsic rocks of the Kara orogen. Blue field—concentrations for syncollisional granitoids from [54,66]. Yellow fields are postcollisional subalkaline granites and granodiorites from [13]. Grey fields are Siberian LIP alkaline syenites from [34]. Dark grey lines are Siberian LIP felsic rocks from [56]. UCC and LCC—upper and lower continental crust data from [100]. Chondrite and primitive mantle values are from [101] and [102], respectively.

Major and trace elements compositions of the studied igneous rocks are in good agreement with published data for the late Paleozoic collisional granites of Northern Taimyr [54,66] (Figures 9–12). Taking these data into account, it seems that in addition to alkali-calcic types, the postcollisional suite also contains alkalic rocks, similar to the plume-related Early and Middle Triassic monzodiorites, monzonites,

syenites and quartz syenites of Northern Taimyr [34,56] (Figure 10). The latter (granites, quartz monzonites and syenites) are metaluminous varieties of the alkalic series with higher concentrations of Ba, K, Sr, La, Ce, Nd, P, Sm, Tb, and Yb than in the majority of the postcollisional rocks (Figures 10–12).

6.2. Zircons Morphology and Internal Structure

The morphology and internal structures of the analyzed grains are displayed on Figures 13–15.

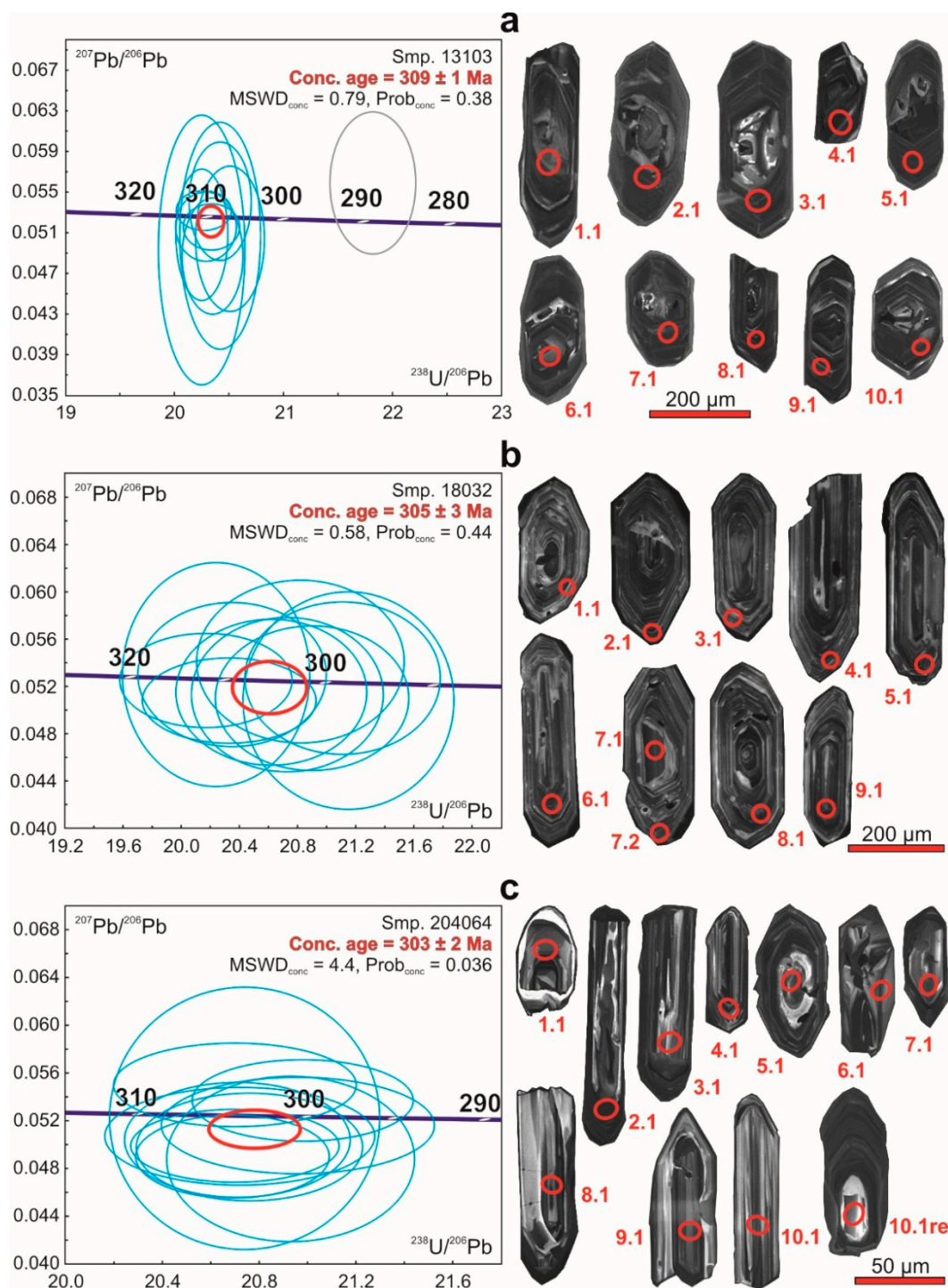


Figure 13. Concordia diagrams and CL zircon images for samples of the first generation of syncollisional granitoids of the Kara orogen: sample 13103 (a), sample 18032 (b), sample 204064 (c). Data-point error ellipses are 2s; decay-const. errs included.

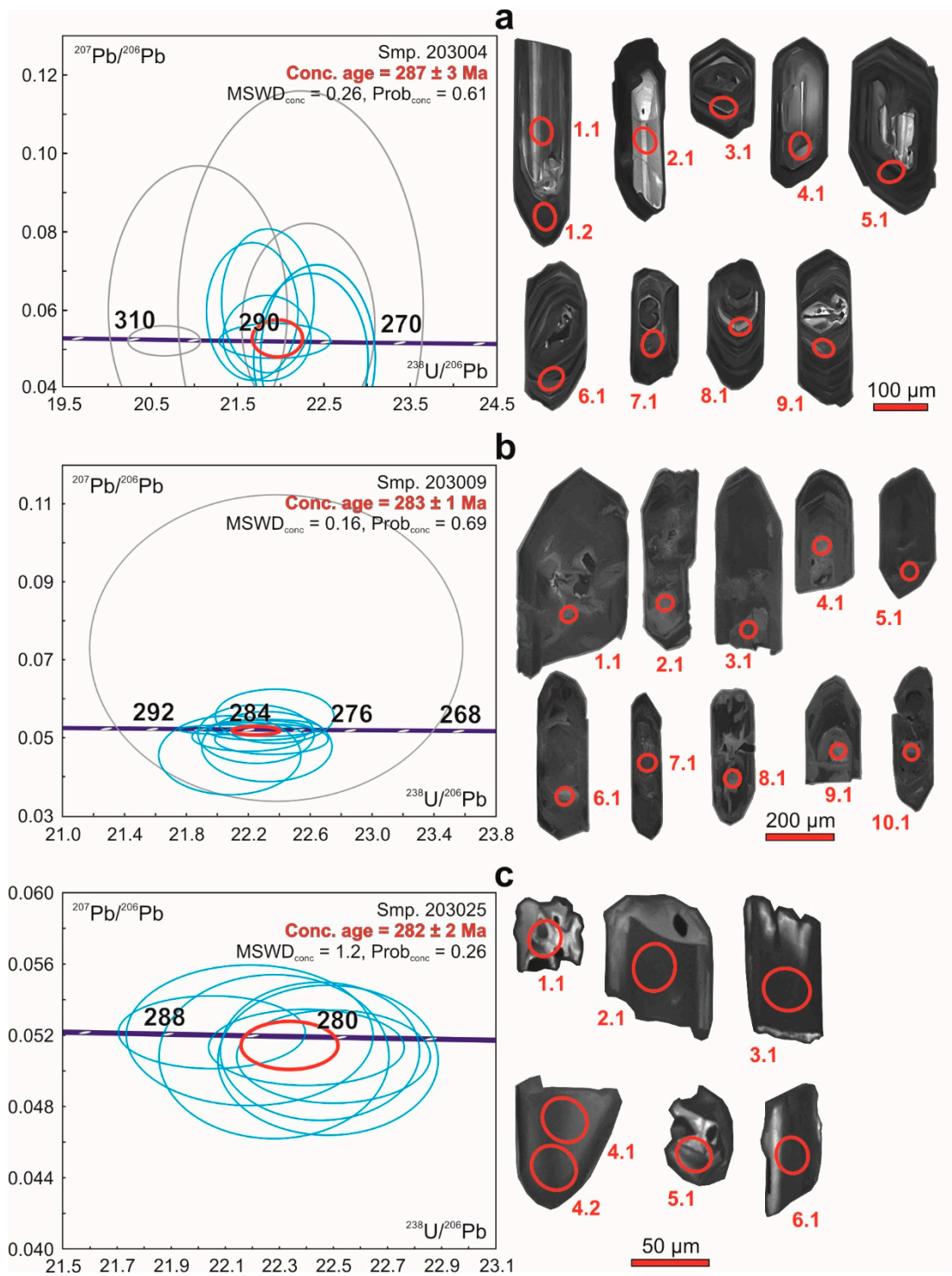


Figure 14. Concordia diagrams and CL zircon images for samples of the second generation of syncollisional granitoids of the Kara orogen: sample 203004 (a), sample 203009 (b), sample 203025 (c). Data-point error ellipses are 2s; decay-const. errs included.

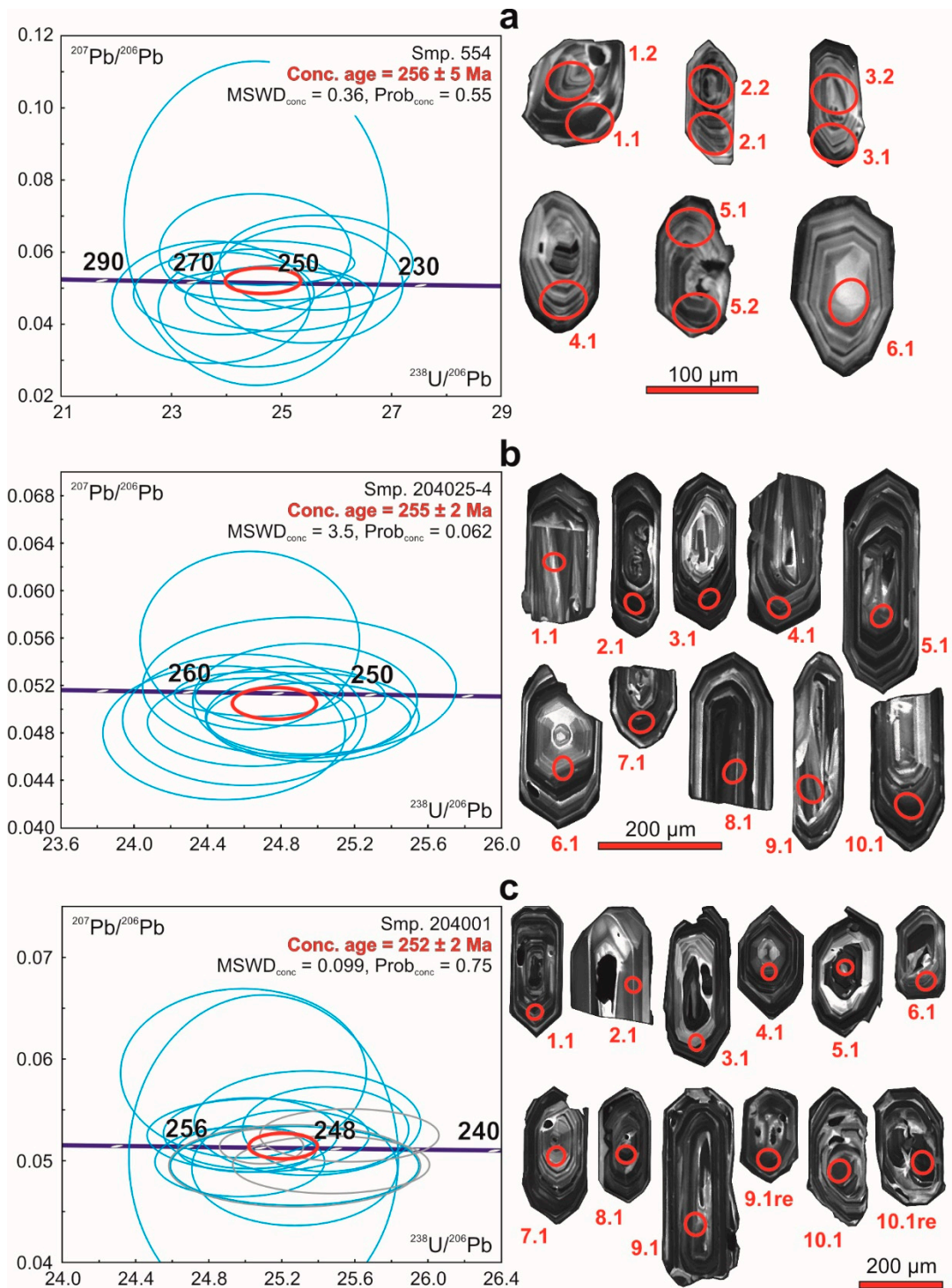


Figure 15. Concordia diagrams and CL zircon images for samples of postcollisional granitoids of the Kara orogen: sample 554 (a), sample 204025-4 (b), sample 204001 (c). Data-point error ellipses are 2 σ ; decay-const. errs included.

Sample 13103. The zircon population comprises mainly subhedral grains, the majority of which are fractured and contain numerous inclusions. The zircons are colorless to brown, transparent to translucent, and faceted mainly by prisms and pyramids, whereas bipyramids are subordinate. Concentric growth zoning can be seen in transmitted light photographs and in CL images. The above features imply the zircons are of magmatic origin.

Sample 18032. The zircons are euhedral to subhedral, elongated, transparent, colorless to pink. Facets are two prisms with (101) pyramid and bipyramids. The zircons contain numerous acicular mineral inclusions, along with melt inclusions of various shapes. Fine oscillatory growth zoning is prevalent, with convolute type locally observed in central domains. These features point to their magmatic origin.

Sample 204064. The zircons are dominantly euhedral to subhedral, transparent, colorless to pink and elongated. Variably shaped polyphase melt inclusions are common, some fractures follow the crystallographic forms, marking concentric growth zoning. CL images display fine to moderately broad bands of concentric growth zoning, with convolute zones around large inclusions. Some structurally disconformable patches are observed, probably as a result of a grain break up, although others may be somewhat rounded fragments of xenocrysts.

Sample 203004. The zircon population comprises euhedral to subhedral grains, transparent to translucent, pinkish to brown in color. The grains are fractured and contain some solid-phase inclusions. CL images demonstrate the presence of disconformable domains surrounded by rims of variably pronounced fine oscillatory zoning, with the outermost bands being CL-dark (non-zoned). Some of them contain inherited cores. The zircon grains features imply their magmatic genesis.

Sample 203009. The zircons are euhedral to subhedral elongated bi-pyramid-prismatic grains with both pyramidal and dipyramidal faces, transparent to translucent, and colorless to brown. The zircons contain various inclusions and have fractures, marking oscillatory growth zoning as well as some irregular fractures. CL imaging reveals the weakly pronounced growth zoning of oscillatory concentric and patchy types, suggesting a magmatic origin.

Sample 203025. Only six fragments of transparent colorless, apparently grains were obtained from this sample. They demonstrate rather weak to no internal CL zoning, suggesting a rapid growth, which is supported by the presence of relatively large melt inclusions. These features imply a magmatic origin.

Sample 554. This sample is dominated by euhedral to subhedral, short to moderately long grains, faceted by combinations of two prisms, pyramids and bipyramids. The zircons are commonly transparent and light-colored. Faint concentric growth zoning is locally observed in transmitted light, whereas bubble- and needle-shaped inclusions are common, but fractures are rather sparse. CL images reveal the prevalence of medium-broad concentric growth zoning, with some central parts having somewhat rounded outlines that most probably resulted from partial resorption of the early zircon nuclei. These features suggest their growth from a melt.

Sample 204025-4. The majority of the zircons are of elongate habit, transparent, colorless to pink. Facets are formed by two prisms with (101) pyramids and bipyramids. The zircons contain numerous acicular and stubby mineral inclusions along with melt inclusions of various shapes. Fine to intermediate broad-banded oscillatory growth zoning supports their magmatic origin.

Sample 204001. The zircons are dominantly euhedral, transparent, light to brownish-colored with two prisms and (101) pyramids. Acicular mineral and variably shaped melt inclusions are common. The inner CL images commonly reveal concentric, fine to moderately broad banding, indicative of their magmatic origin.

6.3. Zircon U–Pb Dating

Sample 13103. Among the ten analytical spots, no. 3.1 yielded a significantly young age, having the lowest U content and the highest Th. This analysis was excluded from the calculations. The other nine analyses form a concordant cluster with an age of 309 ± 1 Ma (MSWD value of 0.79 and a probability of 0.38), which is taken as the crystallization age of the rock (Figure 13a).

Sample 18032. The cluster of 10 analytical spots yields $^{207}\text{Pb}/^{206}\text{Pb}$ and $^{238}\text{U}/^{206}\text{Pb}$ ratios that are concordant. The concordia age is 305 ± 3 Ma (MSWD = 0.58 and probability = 0.44). The cluster can be divided in two groups: if the four youngest (5.1, 9.1, 7.2, 7.1) with some of the lowest $^{206}\text{Pb}^*$ values are excluded, the remaining ones (8.1, 1.1, 4.1, 2.1, 3.1, 6.1) form a concordant cluster with a slightly older age of 309 ± 3 Ma, an MSWD of 0.78 and a probability of 0.38, although this overlaps within error of

the total population. Since there is no obvious anomaly in any of the results, and since the difference between two ages falls in the margin of error, we take total concordia age to be the best estimate of the crystallization age of the rock (Figure 13b).

Sample 204064. Analytical spot 1.1 has a very high $^{206}\text{Pb}^*$ content and yielded a middle Paleoproterozoic age. The zircon's morphology clearly indicates it is a xenocryst. Ten analytical spots from 10 other zircon grains yielded concordant $^{207}\text{Pb}/^{206}\text{Pb}$ and $^{238}\text{U}/^{206}\text{Pb}$ ratios and form a cluster with an MSWD equal to 4.4 and probability equal 0.036 and a concordia age of 303 ± 2 Ma, which is taken as the crystallization age of the rock (Figure 13c).

Sample 203004. All ten analytical spots plot on concordia in terms of $^{207}\text{Pb}/^{206}\text{Pb}$ and $^{238}\text{U}/^{206}\text{Pb}$ ratios (Figure 14a). However, there is a significant scatter of ages along the curve. Analyzes 7.1 and 4.1 have to be excluded as they are significantly older than the other results. The remaining eight spots form a cluster with a concordia age of 287 ± 2 Ma, MSWD of 0.34 and probability of 0.56. Excluding two other analyses with the largest error ellipses gives nearly the same age of 287 ± 3 Ma, but a slightly lower MSWD of 0.26 and a probability of 0.61.

Sample 203009. Nine of ten analyses plot on concordia and form a cluster with an age of 283 ± 1 Ma, MSWD of 0.16 and probability of 0.69 (Figure 14b). Spot 8.1 has an anomalously high $^{207}\text{Pb}/^{206}\text{Pb}$ ratio and % $^{206}\text{Pb}_c$ and was excluded from the calculation.

Sample 203025. Seven analytical spots from six zircon grains yielded $^{207}\text{Pb}/^{206}\text{Pb}$ and $^{238}\text{U}/^{206}\text{Pb}$ ratios close to concordant and form a cluster with a concordia age of 282 ± 2 Ma (Figure 14c). The MSWD value is 1.2, and the probability is 0.26. The concordia age is taken as the crystallization age for this rock.

Sample 554. Ten analytical spots yielded $^{207}\text{Pb}/^{206}\text{Pb}$ and $^{238}\text{U}/^{206}\text{Pb}$ ratios close to concordant and form a cluster with a concordia age of 256 ± 5 Ma (Figure 15a). The MSWD value is 0.36, with a probability of 0.55. There are no significant deviations in isotope ratio values, so we determine this date as the crystallization age for this rock.

Sample 204025-4. Ten analytical spots yielded $^{207}\text{Pb}/^{206}\text{Pb}$ and $^{238}\text{U}/^{206}\text{Pb}$ ratios close to concordant and form a cluster with a concordia age of 255 ± 2 Ma (Figure 15b). Spots 2.1, 3.1 and 4.1 (all taken from zircon rims) show elevated U contents. The MSWD value of 3.5 is somewhat high with a probability of 0.062. The concordia age is taken as the crystallization age for this rock.

Sample 204001. Among the twelve analytical spots, three (6.1, 4.1, 1.1) yielded anomalously young ages. The other nine spots form a concordant cluster with a concordia age of 252 ± 2 Ma, MSWD value of 0.099 and a probability of 0.75 (Figure 15c).

6.4. $^{40}\text{Ar}/^{39}\text{Ar}$ Dating

In biotite and amphibole spectra of diorite sample 541-1 and the same minerals for diorite sample 541-7, four distinct age plateaus can be determined (Figure 16). They are characterized by the release of 67–97% of cumulative ^{39}Ar . Middle Triassic (Anisian) ages for biotite (245.1 ± 2.6 Ma and 247.8 ± 2.6 Ma) for samples 541-1 and 541-7, respectively, and for amphibole from sample 541-1 (246.2 ± 2.6 Ma), coincide well within the margin of error. For amphibole from sample 541-7, the date is older (Guadalupian–Lopingian)— 259.5 ± 2.6 Ma.

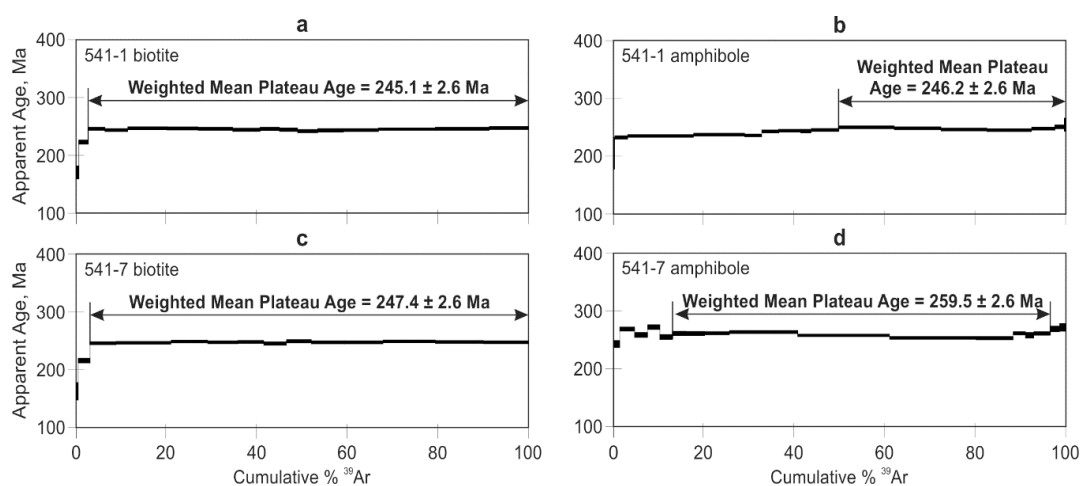


Figure 16. Ar-Ar age spectra for biotite and amphibole from diorite sample 541-1 (a,b) and diorite sample 541-7 (c,d).

7. Discussion

For many years, there have been discussion on how and when did one of the key Arctic structures form at the junction between the Siberian Craton and the Kara microcontinent. New geostructural, geochemical and geochronological data for igneous rocks of the Kara orogen present us with the opportunity to have a deeper understanding of the tectonic processes that manifested along the northern margin of the Siberian Craton in the late Paleozoic to early Mesozoic time. We consider that the late Paleozoic granites and associating acidic and intermediate igneous rocks are, among others, the most useful source of information in this respect.

Our new data have strengthened our opinion that the Kara orogen granites can be divided into syncollisional and postcollisional types [13,32]. Moreover, we are confident that the first group is represented by anatectic granites formed by melting of the crust. It is also clear that various types of material melted in the upper and lower crust—calcareous-greywacke, greywacke, pelitic and basic. This is demonstrated by the variations of petrographic composition of the rocks—from biotite and biotite-hornblende granodiorite and diorite to biotite and two-mica granite and quartz porphyries—as well as by variations in their geochemical composition. These syncollisional granodiorites and granites are peraluminous and correspond to rocks of the calc-alkalic and alkali-calcic magmatic series with Na content exceeding K. That the formation of the syncollisional granites is related to crustal melting is confirmed by the R1–R2 discrimination diagram after [103] (Figure 17), on which these granites plot in the zone of anatectic granitic melts.

In contrast, the postcollisional biotite and biotite-amphibole granodiorites, subalkaline granites, granite-porphyries, quartz syenites and monzonites are weakly peraluminous to weakly metaluminous and belong to the alkali-calcic and alkalic magmatic series and are enriched in K and total alkalis, and slightly enriched in Ba and Sr. On the same diagram (Figure 17) the postcollisional rocks from this study and from published data [13,50] clearly form a trend from the field of anatectic granitic melts towards monzonite and monzodiorite, with elevated alkalinity.

On the MALI vs SiO₂ diagram by [98] (ref. Figure 10), the syncollisional Kara orogen granites plot mostly in the S-type field, and the postcollisional ones—mostly in the A-type field, however both groups significantly overlap the I-type field.

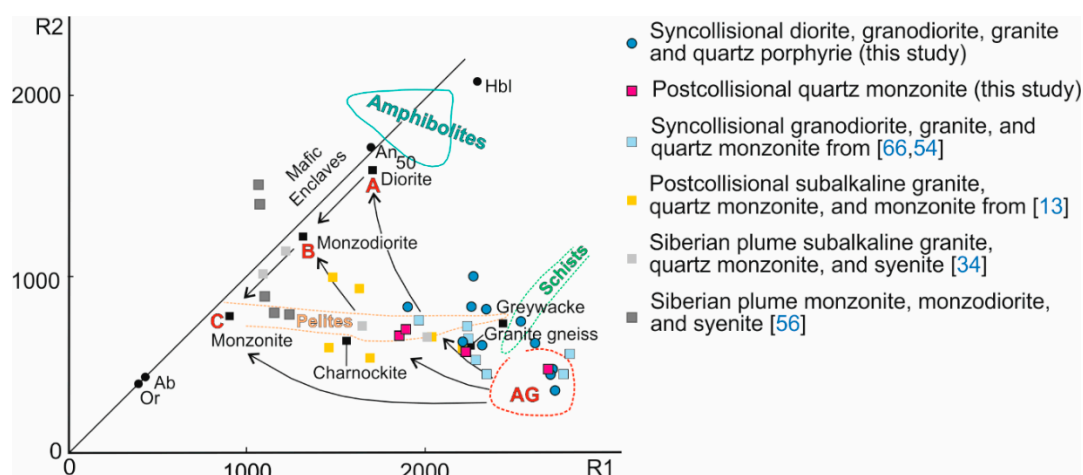


Figure 17. Petrogenetic discrimination diagram R1–R2 for the studied felsic rocks after [103]. $R1 = 4Si - 11(Na + K) - 2(Fe + Ti)$; $R2 = 6Ca + 2Mg + Al$. Components present in cationic proportions. AG—zone of anatectic granitic melts. The vectors AG-A, AG-B and AG-C indicate the change in melt composition under progressive equilibrium partial melting of rocks of dioritic, monzodioritic or monzogranitic bulk composition, respectively (Hbl—Hornblende; An₅₀—Plagioclase (An₅₀); Ab—Albite; Or—Orthoclase). Black squares are central compositional points of imaged rocks. Metasedimentary rocks and amphibolites compositions are from [104].

An even more significant overlap of the studied compositions of granitoids is observed on the discrimination diagrams from [105,106] (Figure 18), that use relationships between contents of Nb and Y, Ta and Yb, Rb and (Nb + Y). On the (Nb + Y) vs Rb diagram, the granitoids mostly occupy the field of postcollisional granites, which can indicate the diversity of their crustal magmatic sources. The latter is corroborated by the similarity in concentrations of most high field strength elements, including Ta, Nb, Y and Yb in the studied intrusive rocks with those concentrations from the upper and lower crust by [100] as seen by their distributions (Figure 12b,d).

Our new U-Pb data for zircon (SHRIMP-II SIMS) obtained for the Kara orogen leads us to divide the granitoids into three age groups: late Carboniferous syncollisional with ages of 309 ± 1 Ma, 305 ± 3 Ma and 303 ± 2 Ma; early Permian with ages of 287 ± 3 Ma, 283 ± 1 Ma and 282 ± 2 Ma; and late Permian postcollisional with ages of 256 ± 5 , 255 ± 2 Ma and 252 ± 2 Ma. Taking into consideration the previously published data for the ages of these granitoids [13,32,50–53], the following age groups can be determined: 315–304 Ma, 287–282 Ma and 264–248 Ma. Thus, the interval between the three main pulses of granitoid magmatism is approximately 20 m.y. In our opinion, this corresponds to a single continent-microcontinent collisional process.

Granitic magmatism began due to the collision of continental masses, with thickening of the crust, accompanied by folding that migrated to the south (in present-day geographic coordinates). However, strike-slip processes were dominating, and the interaction between Siberia and the Kara microcontinent was an oblique collision [20,22,35,67]. The Kara microcontinent continued to rotate counterclockwise relative to Siberia and to slide along the margin of Siberia (Figure 19), which is what probably caused the second magmatic pulse. The formation of postcollisional intrusions took place after the Kara microcontinent had slowed down significantly in relation to the Siberian paleocontinent. Note that the syncollisional granites were emplaced in the western and central part of the region, and the postcollisional ones were mainly in the eastern part (Cape Chelyuskin). Judging from the Ar-Ar isotope data, the cooling of the collisional granites in the orogen due to the closing temperature for the Ar-Ar system for biotite and amphibole ($350\text{--}500$ °C) lasted until 246–245 Ma (see Figure 16).

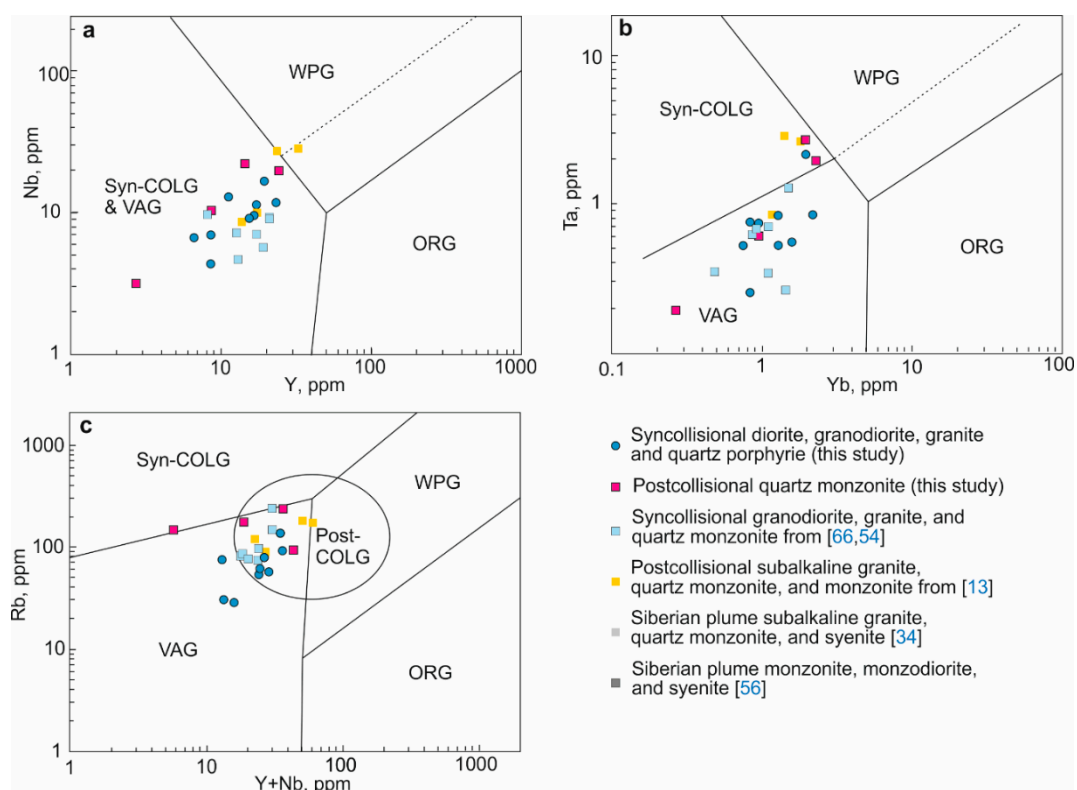


Figure 18. Tectonic setting discrimination diagrams for the granitic rocks: Nb vs. Y (a), Ta vs. Yb (b) from [105] and Rb vs. (Y + Nb) (c) from [106]. VAG = volcanic arc granitoids, ORG = ocean ridge granitoids, WPG = within plate granitoids, Syn-COLG = syncollisional granitoids, Post-COLG = postcollisional granitoids.

It should be noted that at the same time as the postcollisional magmatism was coming to an end (252–248 Ma according to published research and our new U-Pb and Ar-Ar isotope data), the main phase of Siberian plume trap magmatism manifested in the Kara orogen as early as 251–249 Ma (see Figure 1). The age of dolerites and basalts from the Tunguska syncline and of differentiated trap intrusions from Taimyr [45,64] fully correspond to this main phase of the Siberian plume. These bodies, together with individual plutons of syenite and monzonite intruding the trap basalts and collisional granites, formed in the Kara orogen lithosphere that was well-heated by collisional processes in the Early–Middle Triassic [34,42,43,56]. In contrast to the collisional intrusive rocks of the Kara orogen, these monzonites, quartz monzonites and syenites that formed due to the Siberian plume are characterized by a mixed crustal and mantle sources, and are metaluminous and the most enriched in Ba and Sr (see Figures 9–12).

Such a space-time connection of collisional and plume magmatism in the northwestern (Arctic) margin of the Siberian Craton allows us to determine that the plumbing system for magmatic melts of the plume was emplaced due to the oblique collision of the Siberian paleocontinent and the Kara microcontinent in the late Paleozoic along the sutures of the Kara orogen and the Yenisei-Khatanga rift, being the weakest zones of the region. That is to say, this collision became a “trigger” for the outpouring of the Siberian traps at the Permian–Triassic boundary. The structural association of the late-stage Siberian LIP alkaline felsic plutons with old suture zones has been previously described for the Neoproterozoic orogen in the Yenisei Ridge [107].

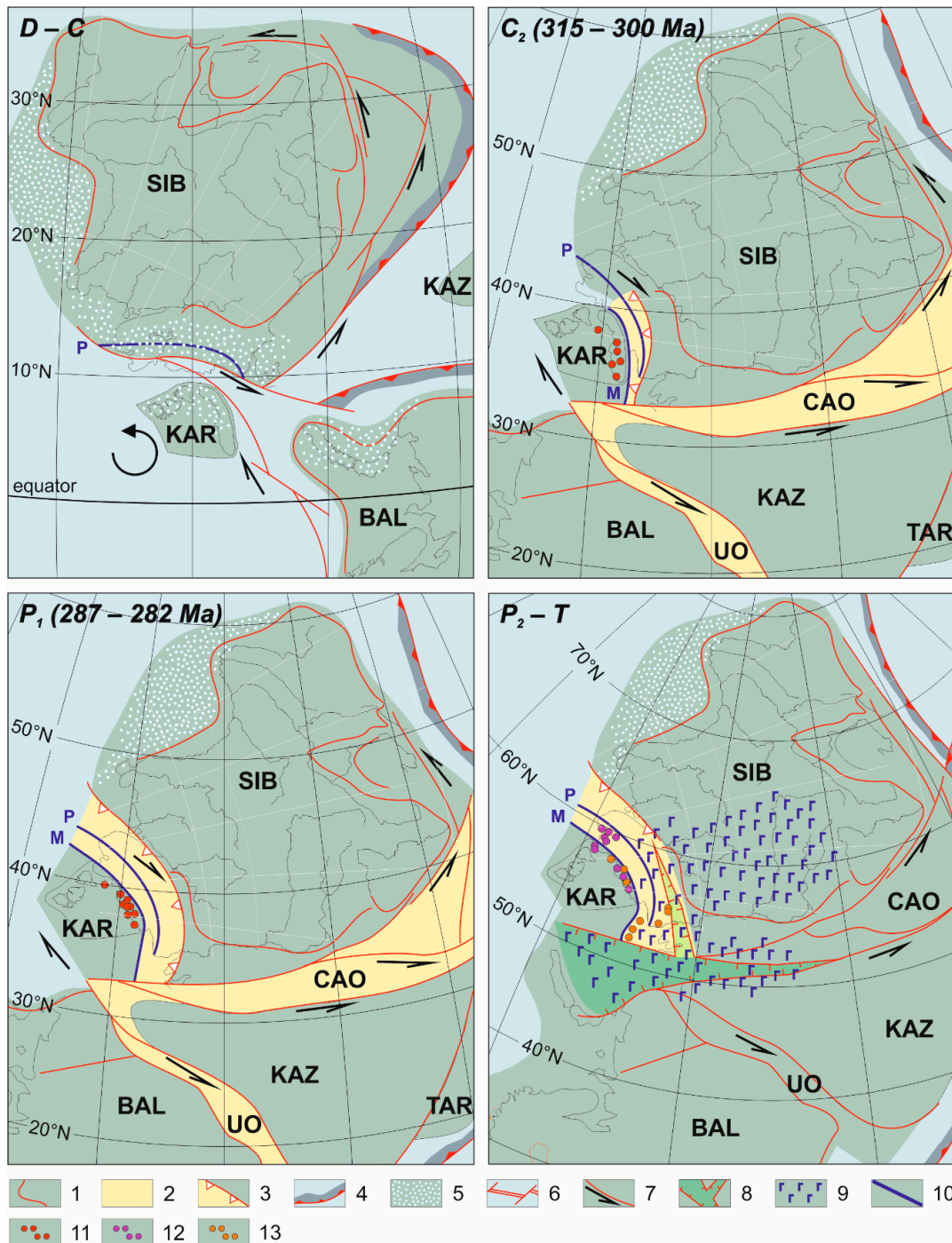


Figure 19. Paleotectonic reconstructions of the formation of the Kara orogen modified from [35]. 1—contours of continental blocks; 2—orogens in formation; 3—orogens deformation front; 4—subduction systems including volcanic belts and back arc basins; 5—passive continental margin shelf; 6—inferred spreading axes; 7—transform margins with kinematics; 8—West Siberian rift system; 9—Siberian traps; 10—sutures in the Arctic margin of Siberia; 11—syncollisional granitoids (315–282 Ma); 12—postcollisional granitoids (264–252 Ma); 13—subalkaline and alkaline felsic plutons (T_{1–3}). Letter abbreviations: continental blocks: SIB—Siberia, KAR—Kara, BAL—Baltica, KAZ—Kazakhstan, TAR—Tarim; orogens: UO—Uralian orogenic belt, CAO—Central Asian orogenic belt; sutures: P—Pyasina-Faddey (NP₃), M—Main Taimyr (Pz).

At the same time, there is still a discussion in the literature on the questions concerning the time of collision between the Siberian paleocontinent and the Kara microcontinent that were formulated over 30 years ago (e.g., [12,13,16,17,19,20,23,25,27,53,63,73,108–111]). The authors participating in the discussion believed that up until the Middle Jurassic, the South Anyui basin—a bay of the Paleo-Pacific Ocean (Panthalassa)—existed and separated the Chukotka and Kara continental units from Siberia. Chukotka and Kara both were parts of the Arctida continent at the time, as proposed by [16,17]. These authors were of the opinion that this part of Arctida collided with Paleo-Siberia only in the Mesozoic, which led to the formation of the fold-and-thrust structure of Southern Taimyr, to deformation of the Early Triassic traps and of the Jurassic sediments at Cape Tsvetkov in Eastern Taimyr.

As we have shown above, the occurrence of Early Triassic dolerite dikes of the Siberian plume traps in the entire orogen (Southern, Central and Northern tectonostratigraphic domains), including Northern Taimyr and Severnaya Zemlya, as well as the existence of Early–Late Triassic syenites and monzonites in Northern Taimyr, introduce additional constraints for paleogeodynamic reconstructions of this region. This information, together with paleomagnetic data [19,20], contradicts the proposed existence of an oceanic bay between the Siberian paleocontinent and the Kara microcontinent until the Middle Jurassic. Our studies show that by the Permian–Triassic boundary, when the Siberian plume magmatism was initiated, the Siberian paleocontinent and the Kara microcontinent already formed a single unit.

The causes of deformation of the trap complex and the Jurassic sediments of Cape Tsvetkov can probably be found in the kinematics of adjacent structures. In the Late Jurassic, deformation in the Verkhoyansk fold belt had begun due to the collision of the Kolyma-Omolon superterrane with the Siberian paleocontinent [15]. These events might have caused compressional deformation in the Taimyr–Severnaya Zemlya fold-and-thrust belt [112,113]. The Amerasian Basin is considered to have opened during the Early Jurassic–Early Cretaceous [114–116], whereas from the other side of Siberia, the West Siberian basin began forming due to a system of north-south trending rift systems, causing compressional deformation in the Kara orogen.

8. Conclusions

Our new geostructural, geochemical, geochronological data for igneous rocks of the Kara (Taimyr-Severnaya Zemlya) orogen, when combined with the analysis of published research results, allow us to present a number of conclusions based on all of these studies:

1. The late Carboniferous–Permian granitoids widely represented in the Kara orogen were formed due to oblique collision of the Siberian paleocontinent and the Kara microcontinent;
2. The syncollisional granites (315–282 Ma) were formed in areas of anatexis melting of crustal material and were localized mainly in zones of amphibolite metamorphism and migmatization. They are mostly peraluminous biotite-hornblende granodiorites or porphyroblastic biotite-amphibole and two-mica granites, with characteristics of the calc-alkalic and alkali-calcic magmatic series;
3. The postcollisional granites (264–248 Ma) form mainly small stocks intruding metamorphic rocks and syncollisional granites, along with unmetamorphosed Paleozoic cover deposits in the Central Domain. They are biotite-amphibole granodiorites, subalkaline granites, granite-porphyrries, quartz syenites and monzonites, weakly peraluminous to weakly metaluminous, and belong to the alkali-calcic and alkalic magmatic series. These rocks are enriched in K and total alkalis and slightly enriched in Ba and Sr.
4. The granites of the Kara orogen can be divided into three age groups:
 - (a) syncollisional late Carboniferous—315–304 Ma;
 - (b) syncollisional early Permian—287–282 Ma;
 - (c) postcollisional late Permian—264–248 Ma.

The duration of granite formation corresponds to one single collisional process of the continent-microcontinent type. We explain the 20 m.y. time gap between magmatic pulses in the late Carboniferous and the early Permian to the effect of the continuing counterclockwise rotation of the Kara microcontinent relative to Siberia, while at the same time sliding along its margin.

5. At the same time as the postcollisional magmatism was ending, in the Early Triassic, differentiated and individual intrusions related to the Siberian plume began intruding the lithosphere of the Kara orogen that was well-heated through collisional processes. They are metaluminous monzonites, quartz monzonites and syenites with a mixed crustal-mantle source, characteristic of the calc-alkalic and alkalic magmatic series and are the most enriched in Ba and Sr.
6. The oblique collision of the Siberian paleocontinent and the Kara microcontinent at the end of the Paleozoic led to the opening of the plumbing system for the magmatic melts of the Siberian plume along the sutures of the Kara orogen and the Yenisei-Khatanga rift because these were the weakest zones. Therefore, this collision became a “trigger” for the outpouring of the Siberian traps at the Permian–Triassic boundary.
7. The occurrence of Early Triassic dolerite dikes of the Siberian plume traps across the entire orogen (Southern, Central and Northern tectonostratigraphic domains), including Northern Taimyr and Severnaya Zemlya, as well as the existence of Early–Late Triassic syenites and monzonites in northern Taimyr, introduce additional constraints for the paleogeodynamic reconstruction of this region. Our studies show that by the Permian–Triassic boundary, when the Siberian plume magmatism was initiated, the Siberian paleocontinent and the Kara microcontinent had already formed a single unit.

Author Contributions: Conceptualization, V.A.V., V.P.; methodology, V.A.V., V.P., A.V.; validation, V.A.V., A.V., A.L., A.T.; formal analysis, A.L., A.T., N.M., P.K.; investigation, V.A.V., A.V., V.P., N.M., M.P., A.L., A.T.; resources, V.A.V., V.P.; data curation, V.A.V., V.P., M.P.; writing—original draft preparation, V.A.V., V.P., A.V., N.M., M.P., A.L., and A.T.; writing—review and editing, V.A.V., N.M.; visualization, P.K., N.M.; supervision, V.A.V.; project administration, V.A.V., V.P.; funding acquisition, V.A.V., V.P. All authors have read and agreed to the published version of the manuscript.

Funding: This research was financially supported by the Russian Science Foundation, grant no. 19-17-00091; and by the Russian Foundation for Basic Research, grants numbers 18-05-70035 and 20-05-00360.

Acknowledgments: We are very grateful to prof. Simon A. Wilde for proofreading the text and helping to greatly improve the quality of the language.

Conflicts of Interest: The authors declare no conflict of interest. The funders had no role in the design of the study; in the collection, analyses, or interpretation of data; in the writing of the manuscript, or in the decision to publish the results.

Appendix A

Table A1. Coordinates and georeferences for the studied samples granitoid samples.

Sample No.	Rock Type	GPS Coordinates	Georeference or Pluton Name	Age, Ma
18032	Granodiorite	N 74°42'57.3" E 86°14'42.0"	Minin cape, Minin pluton	305 ± 3
13103	Granodiorite	N 75°35'25.23" E 94°26'7.39"	Left bank of Kolomeitseva R., NE trending body parallel to the Kolomeitsev pluton	309 ± 1
204064	Biotite granodiorite	N 75°24'56.0" E 93°20'27.7"	Upper reaches of Srenk R., NE trending Kolomeitsev pluton	303 ± 2
203004	Two-mica gneiss-granite	N 75°37'46,6" E 90°52'12,4"	Inland, south of cape Dubinsky and cape Tillo	287 ± 2
203009	Two-mica leuco-gneiss-granite	N 75°23'03,5" E 91°58'18,1"	Lower reaches of Orientirnaya R., right feeder of Kamennaya R.	283 ± 1
203025	Plagiortholite porphyry	N 75°42'17.56" E 95°39'17.19"	Mouth of Spokoynaya R., right feeder of Kolomeitseva R.	282 ± 2
554	Biotite-hornblende subalkaline granite	N 76°32'00.3" E 104°26'29.1"	Upper reaches of Tikhaya R., stock of the Pekin complex	256 ± 5
204025/4	Subalkaline granite	E 75°18'23.56" N 93°58'59.66"	Upper reaches of Shumyashiy creek, Kamenistin pluton, Olenyin complex	255 ± 2
204001	Subalkaline biotite granite	N 75°25'25.0" E 96°20'19.6"	Volchiy pluton, Olenyin complex	252 ± 2

Appendix B

Table A2. Results of X-ray fluorescence and ICP-MS analyses for the studied rocks.

Sample/Component	541-7	541-1	13103	18032	541-2	543-2	204064	541-4	203004	203009	203025	204001	204025/4	204025/4A	554
	1	2	3	4	5	6	7	8	9	10	11	12	13	14	15
SiO ₂ , wt. %	60.71	61.43	65.26	65.7	65.93	66.78	67.00	68.53	72.61	73.57	74.66	66.7	69.5	74.4	74.5
TiO ₂	0.68	0.75	0.77	0.8	0.61	0.55	0.76	0.58	0.47	0.13	0.06	0.56	0.34	0.072	0.07
Al ₂ O ₃	16.52	18.01	16.8	16.7	17	16.66	15.7	15.43	14	15.4	15.7	16.6	15.5	14.2	13.2
Fe ₂ O ₃ *	6.3	5.46	4.46	4.40	4.27	3.63	4.68	4.26	2.81	1.42	1.08	3.23	2.66	1.06	0.81
MnO	0.14	0.14	0.072	0.07	0.12	0.13	0.077	0.13	0.04	0.02	0.02	0.052	0.064	0.018	0.01
MgO	5.98	4.78	1.78	1.72	3.01	3.12	1.79	1.42	0.95	0.72	0.37	1.3	0.82	0.55	3.66
CaO	3.44	2.09	3.52	3.76	1.29	1.08	3.14	3.03	1.39	0.96	0.22	2.5	2.11	1.56	0.96
Na ₂ O	2.92	3.93	3.98	4.39	3.17	3.64	3.24	3.15	3.17	4.01	4.81	3.9	3.58	2.94	3.66
K ₂ O	2.33	2.7	1.88	1.79	3.93	3.09	2.67	2.98	3.88	3.08	2.12	4.71	4.44	5.05	5.33
P ₂ O ₅	0.25	0.25	0.36	0.21	0.2	0.29	0.25	0.17	0.17	0.13	0.05	0.17	0.12	<0.05	0.05
LOI	0.71	0.44	0.26	0.7	0.45	0.99	0.74	0.3	0.48	0.76	1.01	0.51	0.55	0.12	0.47
Total	99.98	99.98	99.5	99.7	99.98	99.96	99.827	99.99	99.81	100.18	100.03	100	99.7	100	102.71
Rb, ppm	45.6	28.2	61.3	57.4	30.6	54.7	78.4	30.5	138	75.3	94.1	92.3	177	143	234
Sr	716	801	486	605	676	513	467	449	107	115	80.1	488	256	265	87.9
Y	14.1	10.80	15.5	17.2	6.58	11.2	16.6	8.49	22.9	8.52	19.5	24.2	8.60	2.67	14.5
Zr	35.5	27.5	174	211	52.5	86.7	245	78.1	138	37.9	46.0	330	149	56.0	68.8
Nb	6.19	5.05	9.26	11.3	6.71	13.0	9.64	6.97	11.9	4.36	16.7	19.8	10.4	3.13	22.1
Cs	1.76	1.15	2.81	2.24	-	-	1.53	-	3.29	1.31	2.16	1.79	4.88	2.13	-
Ba	596	1150	701	820	1620	1290	780	790	280	219	58.3	1360	723	1020	199
La	19.3	20.6	21.7	18.7	31.7	16.4	49.1	27.6	28.1	8.24	6.70	96.2	24.3	7.81	11.3
Ce	42.0	33.6	44.8	39.0	48.1	32.2	93.4	49.3	60.5	18.0	13.7	172	47.8	14.1	23.1
Pr	5.35	5.55	5.67	4.44	7.43	4.33	9.87	6.61	7.21	2.15	1.73	17.0	4.30	1.39	2.45
Nd	20.5	22.7	23.2	18.5	28.7	17.1	35.6	24.7	28.4	8.56	6.67	57.5	14.1	4.39	8.17
Sm	3.77	4.07	5.14	4.64	4.76	3.65	6.29	4.02	6.33	2.04	2.27	8.01	2.62	0.84	1.65
Eu	1.05	1.32	1.47	1.38	1.34	1.34	1.14	1.08	0.64	0.36	0.38	1.74	0.68	0.44	0.25
Gd	3.53	3.46	4.71	3.56	3.73	3.65	5.09	3.20	5.17	1.87	2.34	6.86	2.16	0.53	1.59
Tb	0.55	0.48	0.58	0.55	0.41	0.55	0.58	0.42	0.79	0.26	0.46	0.85	0.26	0.09	0.27
Dy	2.76	2.40	3.19	3.02	1.54	2.39	2.97	1.85	4.18	1.76	3.06	4.30	1.23	0.42	1.73
Ho	0.61	0.55	0.61	0.65	0.29	0.44	0.66	0.34	0.82	0.28	0.66	0.93	0.31	0.09	0.36

Table A2. Cont.

Sample/Component	541-7	541-1	13103	18032	541-2	543-2	204064	541-4	203004	203009	203025	204001	204025/4	204025/4A	554
	1	2	3	4	5	6	7	8	9	10	11	12	13	14	15
Er	1.55	1.31	1.38	1.71	0.75	1.04	1.58	0.85	2.16	0.77	1.65	2.33	0.81	0.24	1.41
Tm	0.23	0.18	0.23	0.28	0.11	0.16	0.24	0.13	0.33	0.13	0.28	0.38	0.13	0.05	0.27
Yb	1.33	1.15	1.29	1.23	0.83	0.94	1.57	0.84	2.13	0.74	1.93	2.28	0.97	0.27	1.91
Lu	0.19	0.17	0.19	0.24	0.09	0.14	0.20	0.12	0.34	0.14	0.27	0.36	0.16	0.06	0.31
Hf	1.19	0.94	4.75	5.20	1.31	2.15	-	2.27	4.26	1.35	2.42	6.79	-	-	3.01
Ta	0.29	0.30	0.52	0.85	0.76	0.75	0.56	0.26	0.84	0.53	2.16	1.95	0.61	0.19	2.68
Th	3.84	2.07	6.04	8.70	4.14	3.86	11.4	5.57	21.1	3.11	10.7	16.2	15.8	2.67	19.0
U	2.25	0.35	1.84	1.73	0.79	1.42	1.83	0.90	4.46	3.83	7.74	1.95	2.63	0.81	8.19
Na ₂ O + K ₂ O	5.25	6.63	5.86	6.18	7.10	6.73	5.91	6.13	7.05	7.09	6.93	8.61	8.02	7.99	8.99
Na ₂ O/K ₂ O	1.25	1.46	2.12	2.45	0.81	1.18	1.21	1.06	0.82	1.30	2.27	0.83	0.81	0.58	0.69
(La/Yb) _N	9.79	12.09	11.35	10.26	25.84	11.79	21.11	22.10	8.90	7.52	2.34	28.48	16.91	19.52	3.99
Eu/Eu*	0.88	1.08	0.91	1.04	0.97	1.12	0.62	0.92	0.34	0.56	0.50	0.72	0.87	2.02	0.47
Σ REE	102.72	97.54	114.16	97.90	129.78	79.34	208.29	121.06	147.10	45.30	42.10	370.74	99.83	30.72	54.77

Note: 1–8—syncollisional diorites and granodiorites (309–303 Ma); 9–11—syncollisional granites and quartz porphyry (287–282 Ma); 12–15—postcollisional quartz monzonite, granites (256–252 Ma). Elements contents are normalized according to [101]: Eu/Eu* = (Eu_{CN})/(Sm_{CN}·Gd_{CN})^{0.5}; LOI—loss on ignition.

Appendix C

Table A3. Results of geochronological studies of the collisional granites of the Kara orogen.

Spot No.	Content, ppm					Isotope ratios				Err. Corr.	Age (Ma) (1) ²⁰⁶ Pb/ ²³⁸ U (±%)
	U	Th	²⁰⁶ Pb*	²³² Th/ ²³⁸ U	% ²⁰⁶ Pb _c	(1)	(1)	(1)	(1)		
						²³⁸ U/ ²⁰⁶ Pb*	²⁰⁷ Pb*/ ²⁰⁶ Pb*	²⁰⁷ Pb*/ ²³⁵ U	²⁰⁶ Pb*/ ²³⁸ U		
Sample 13103 (concordia age = 309 ± 1 Ma, MSWD (concordance) = 0.79, probability = 0.38)											
3.1	788	472	31.1	0.62	0.22	21.82 ± 0.71	0.0559 ± 5	0.353 ± 5	0.04582 ± 0.71	0.142	288.8 ± 2
9.1	1693	283	72.3	0.17	1.96	20.51 ± 0.63	0.0504 ± 5.8	0.339 ± 5.8	0.04874 ± 0.63	0.108	306.8 ± 1.9
10.1	1588	239	69.3	0.16	3.57	20.42 ± 0.74	0.0507 ± 9	0.342 ± 9.1	0.04893 ± 0.74	0.082	307.9 ± 2.2
1.1	1046	262	44.3	0.26	0.63	20.42 ± 0.57	0.0541 ± 4.4	0.365 ± 4.5	0.04895 ± 0.57	0.129	308.1 ± 1.7
7.1	1326	191	56.2	0.15	0.42	20.35 ± 0.56	0.0487 ± 4.8	0.33 ± 4.8	0.04914 ± 0.56	0.115	309.2 ± 1.7
6.1	1804	294	76.3	0.17	0.10	20.34 ± 0.52	0.05157 ± 1.8	0.3495 ± 1.8	0.04916 ± 0.52	0.283	309.3 ± 1.6

Table A3. Cont.

Spot No.	Content, ppm					Isotope ratios				Err. Corr.	Age (Ma) (1) $^{206}\text{Pb}/^{238}\text{U}$ ($\pm\%$)
	U	Th	$^{206}\text{Pb}^*$	$^{232}\text{Th}/^{238}\text{U}$	% $^{206}\text{Pb}_c$	(1) $^{238}\text{U}/^{206}\text{Pb}^*$ ($\pm\%$)	(1) $^{207}\text{Pb}^*/^{206}\text{Pb}^*$ ($\pm\%$)	(1) $^{207}\text{Pb}^*/^{235}\text{U}$ ($\pm\%$)	(1) $^{206}\text{Pb}^*/^{238}\text{U}$ ($\pm\%$)		
4.1	1473	203	62.6	0.14	0.41	20.29 \pm 0.56	0.0516 \pm 2.7	0.3509 \pm 2.8	0.04929 \pm 0.56	0.199	310.2 \pm 1.7
8.1	1963	442	86.8	0.23	4.08	20.25 \pm 0.8	0.0493 \pm 11	0.335 \pm 11	0.04934 \pm 0.8	0.075	310.4 \pm 2.4
5.1	1750	274	74.1	0.16	–	20.27 \pm 0.51	0.05318 \pm 1.5	0.3618 \pm 1.6	0.04934 \pm 0.51	0.325	310.5 \pm 1.6
2.1	1611	298	68.7	0.19	0.50	20.252 \pm 0.48	0.0508 \pm 5.2	0.346 \pm 5.2	0.04937 \pm 0.48	0.092	310.7 \pm 1.5
Sample 18032 (concordia age = 305 \pm 3 Ma, MSWD (concordance) = 0.58, probability = 0.38)											
5.1	522	74	21.4	0.15	1.03	21.15 \pm 1.4	0.0508 \pm 7.4	0.331 \pm 7.5	0.04727 \pm 1.4	0.192	298 \pm 4.2
9.1	811	160	33.2	0.20	0.70	21.11 \pm 1.3	0.0527 \pm 5	0.344 \pm 5.1	0.04737 \pm 1.3	0.252	298 \pm 3.8
7.2	831	180	34.4	0.22	0.66	20.9 \pm 1.3	0.051 \pm 4.9	0.336 \pm 5.1	0.04784 \pm 1.3	0.254	301 \pm 3.8
7.1	623	163	25.9	0.27	0.67	20.82 \pm 1.4	0.0541 \pm 5.2	0.358 \pm 5.4	0.04803 \pm 1.4	0.251	302 \pm 4.0
8.1	898	161	37.5	0.19	0.75	20.73 \pm 1.3	0.0513 \pm 5.2	0.341 \pm 5.3	0.04823 \pm 1.3	0.237	304 \pm 3.8
1.1	789	122	33.0	0.16	0.38	20.62 \pm 1.3	0.0515 \pm 4.9	0.344 \pm 5	0.0485 \pm 1.3	0.258	305 \pm 3.9
4.1	953	213	40.5	0.23	0.70	20.35 \pm 1.3	0.053 \pm 4.7	0.359 \pm 4.9	0.04913 \pm 1.3	0.257	309 \pm 3.8
2.1	901	205	38.1	0.23	0.21	20.33 \pm 1.2	0.0508 \pm 2.9	0.345 \pm 3.1	0.04918 \pm 1.2	0.398	310 \pm 3.8
3.1	815	142	35.3	0.18	2.08	20.24 \pm 1.3	0.053 \pm 7.3	0.361 \pm 7.4	0.04938 \pm 1.3	0.179	311 \pm 4.0
6.1	1004	146	42.9	0.15	0.27	20.17 \pm 1.2	0.0525 \pm 3.1	0.359 \pm 3.3	0.04959 \pm 1.2	0.363	312 \pm 3.7
Sample 204064 (concordia age = 303 \pm 2 Ma, MSWD (concordance) = 4.4, probability = 0.036)											
1.1	261	112	84.7	0.44	0.09	2.653 \pm 0.87	0.1267 \pm 0.8	6.585 \pm 1.2	0.3768 \pm 0.87	0.735	2061 \pm 15
2.1	1166	143	48.6	0.13	0.37	20.69 \pm 0.79	0.049 \pm 2.9	0.3268 \pm 3	0.04833 \pm 0.79	0.260	304.3 \pm 2.3
3.1	231	74	9.48	0.33	0.00	20.96 \pm 1.1	0.0516 \pm 3.2	0.339 \pm 3.4	0.04771 \pm 1.1	0.324	300.5 \pm 3.2
4.1	666	222	27.7	0.35	0.18	20.7 \pm 0.85	0.0499 \pm 2.5	0.3325 \pm 2.7	0.0483 \pm 0.85	0.321	304.1 \pm 2.5
5.1	328	175	13.6	0.55	0.00	20.7 \pm 0.99	0.055 \pm 2.6	0.366 \pm 2.8	0.04831 \pm 0.99	0.355	304.1 \pm 3
6.1	537	173	22	0.33	0.16	20.98 \pm 0.89	0.0537 \pm 2.6	0.353 \pm 2.7	0.04766 \pm 0.89	0.329	300.1 \pm 2.6
7.1	354	300	14.6	0.87	0.36	20.93 \pm 1	0.0488 \pm 5.8	0.321 \pm 5.9	0.04778 \pm 1	0.173	300.9 \pm 3
8.1	402	190	16.7	0.49	0.53	20.74 \pm 1.1	0.0522 \pm 8.6	0.347 \pm 8.7	0.04821 \pm 1.1	0.124	303.5 \pm 3.2
9.1	503	184	20.9	0.38	0.20	20.71 \pm 0.92	0.0504 \pm 3.9	0.335 \pm 4	0.04828 \pm 0.92	0.230	304 \pm 2.7
10.1	493	201	20.5	0.42	0.30	20.76 \pm 0.92	0.0498 \pm 3.7	0.331 \pm 3.8	0.04816 \pm 0.92	0.245	303.2 \pm 2.7
10.RE	230	153	9.56	0.69	0.03	20.72 \pm 1.1	0.0507 \pm 3.3	0.337 \pm 3.4	0.04826 \pm 1.1	0.322	303.8 \pm 3.3

Table A3. Cont.

Spot No.	Content, ppm					Isotope ratios				Err. Corr.	Age (Ma) (1) $^{206}\text{Pb}/^{238}\text{U}$ ($\pm\%$)
	U	Th	$^{206}\text{Pb}^*$	$^{232}\text{Th}/^{238}\text{U}$	% $^{206}\text{Pb}_c$	(1) $^{238}\text{U}/^{206}\text{Pb}^*$ ($\pm\%$)	(1) $^{207}\text{Pb}^*/^{206}\text{Pb}^*$ ($\pm\%$)	(1) $^{207}\text{Pb}^*/^{235}\text{U}$ ($\pm\%$)	(1) $^{206}\text{Pb}^*/^{238}\text{U}$ ($\pm\%$)		
Sample 203004 (concordia age = 287 ± 3 Ma, MSWD (concordance) = 0.26, probability = 0.61)											
5.1r	3616	263	177	0.08	21.57	22.32 ± 1.4	0.056 ± 19	0.339 ± 19	0.04433 ± 1.4	0.077	279.6 ± 3.9
8.1c	1219	506	62.2	0.43	24.25	22.23 ± 2.6	0.06 ± 38	0.36 ± 38	0.0442 ± 2.6	0.068	279 ± 7.1
6.1r	2008	212	95.8	0.11	19.73	22.43 ± 1.2	0.048 ± 20	0.294 ± 20	0.04451 ± 1.2	0.059	280.7 ± 3.2
1.2r	2336	276	115	0.12	22.07	22.35 ± 1.2	0.0473 ± 19	0.291 ± 19	0.04468 ± 1.2	0.062	281.8 ± 3.3
3.1r	2312	718	106	0.32	13.97	21.85 ± 1	0.0624 ± 12	0.389 ± 12	0.04531 ± 1	0.084	285.7 ± 2.9
2.1c	192	81	7.51	0.43	0.00	21.93 ± 1.2	0.0522 ± 3.5	0.328 ± 3.7	0.04559 ± 1.2	0.311	287.4 ± 3.3
1.1c	696	520	27.7	0.77	1.14	21.84 ± 0.95	0.0529 ± 8.4	0.334 ± 8.5	0.04578 ± 0.95	0.112	288.6 ± 2.7
9.1c	1693	260	76.5	0.16	12.26	21.67 ± 1	0.0597 ± 12	0.376 ± 12	0.0458 ± 1	0.087	288.7 ± 2.9
7.1c	1626	370	80.6	0.23	17.57	21.04 ± 2	0.06 ± 25	0.389 ± 25	0.04699 ± 2	0.081	296 ± 5.9
4.1c	622	585	25.9	0.97	0.23	20.65 ± 0.82	0.0522 ± 2.9	0.348 ± 3	0.04842 ± 0.82	0.276	304.8 ± 2.4
Sample 203009 (concordia age = 283 ± 1 Ma, MSWD (concordance) = 0.16, probability = 0.69)											
8.1	1729	5	127	0.003	47.63	22.38 ± 2.2	0.073 ± 22	0.441 ± 22	0.04373 ± 2.2	0.098	275.9 ± 5.8
4.1	2363	2	97.6	0.001	7.04	22.37 ± 0.7	0.0555 ± 5.1	0.341 ± 5.1	0.04462 ± 0.7	0.137	281.4 ± 1.9
2.1	2420	21	95.1	0.009	2.14	22.35 ± 0.67	0.0496 ± 3.2	0.3057 ± 3.3	0.04473 ± 0.67	0.206	282.1 ± 1.9
6.1	1371	1	56.2	0.001	6.04	22.32 ± 0.77	0.0477 ± 7.7	0.294 ± 7.7	0.04473 ± 0.77	0.100	282.1 ± 2.1
9.1	1778	1	68.6	0.001	0.14	22.31 ± 0.66	0.0525 ± 1.7	0.3244 ± 1.8	0.04481 ± 0.66	0.367	282.6 ± 1.8
7.1	2890	3	121	0.001	7.79	22.25 ± 0.69	0.0509 ± 6	0.315 ± 6	0.04486 ± 0.69	0.115	282.9 ± 1.9
3.1	3191	9	125	0.003	1.40	22.27 ± 0.63	0.0519 ± 2	0.3213 ± 2.1	0.04488 ± 0.63	0.301	283 ± 1.8
1.1	1980	2	78.2	0.001	1.95	22.2 ± 0.67	0.0502 ± 3	0.3114 ± 3.1	0.04503 ± 0.67	0.216	283.9 ± 1.9
10.1	1133	3	48.6	0.003	9.19	22.08 ± 0.85	0.0455 ± 9.1	0.283 ± 9.1	0.04518 ± 0.85	0.093	284.9 ± 2.4
5.1	3200	2	124	0.001	0.04	22.09 ± 0.62	0.05204 ± 0.97	0.3248 ± 1.2	0.04527 ± 0.62	0.536	285.4 ± 1.7
Sample 203025 (concordia age = 282 ± 2 Ma, MSWD (concordance) = 1.2, probability = 0.26)											
2.1	1061	594	40.6	0.58	0.25	22.5 ± 0.65	0.0508 ± 2.1	0.311 ± 2.2	0.04444 ± 0.65	0.302	280.3 ± 1.8
5.1	710	250	27.3	0.36	0.47	22.48 ± 0.74	0.0506 ± 3.4	0.311 ± 3.4	0.04448 ± 0.74	0.215	280.6 ± 2
4.2	1361	476	52.6	0.36	0.91	22.45 ± 0.67	0.0511 ± 3.1	0.3141 ± 3.1	0.04454 ± 0.67	0.213	280.9 ± 1.8
3.1	999	566	38.3	0.59	0.04	22.4 ± 0.66	0.05132 ± 1.7	0.3159 ± 1.9	0.04464 ± 0.66	0.356	281.6 ± 1.8
6.1	1275	579	49.9	0.47	1.43	22.28 ± 0.78	0.0508 ± 3.7	0.314 ± 3.8	0.04488 ± 0.78	0.205	283 ± 2.1
1.1	400	97	15.5	0.25	0.18	22.19 ± 0.84	0.052 ± 3.1	0.323 ± 3.2	0.04507 ± 0.84	0.266	284.2 ± 2.3
4.1	1209	577	47.2	0.49	0.09	22.05 ± 0.64	0.05217 ± 1.6	0.3262 ± 1.7	0.04535 ± 0.64	0.369	285.9 ± 1.8

Table A3. Cont.

Spot No.	Content, ppm					Isotope ratios				Err. Corr.	Age (Ma) (1) $^{206}\text{Pb}/^{238}\text{U}$ ($\pm\%$)
	U	Th	$^{206}\text{Pb}^*$	$^{232}\text{Th}/^{238}\text{U}$	% $^{206}\text{Pb}_c$	(1) $^{238}\text{U}/^{206}\text{Pb}^*$ ($\pm\%$)	(1) $^{207}\text{Pb}^*/^{206}\text{Pb}^*$ ($\pm\%$)	(1) $^{207}\text{Pb}^*/^{235}\text{U}$ ($\pm\%$)	(1) $^{206}\text{Pb}^*/^{238}\text{U}$ ($\pm\%$)		
Sample 554 (concordia age = 256 ± 5 Ma, MSWD (concordance) = 0.36, probability = 0.55)											
1.1	403	718	13.8	1.84	1.72	25.46 ± 2.8	0.051 ± 13	0.276 ± 13	0.0393 ± 2.8	0.213	248.3 ± 6.8
1.2	226	378	7.84	1.73	–	24.52 ± 2.9	0.06 ± 11	0.338 ± 12	0.0408 ± 2.9	0.253	257.8 ± 7.4
2.1	287	228	10	0.82	0.00	24.69 ± 2.7	0.0509 ± 3.5	0.284 ± 4.4	0.0405 ± 2.7	0.614	256 ± 6.8
2.2	299	262	10.1	0.91	1.32	25.63 ± 2.8	0.0571 ± 9.4	0.307 ± 9.8	0.039 ± 2.8	0.287	246.6 ± 6.8
3.1	245	290	8.48	1.22	0.40	24.96 ± 2.8	0.0472 ± 7.9	0.261 ± 8.4	0.0401 ± 2.8	0.335	253.2 ± 6.9
3.2	115	153	4.2	1.38	1.17	23.72 ± 3.1	0.0461 ± 15	0.268 ± 15	0.0422 ± 3.1	0.204	266.2 ± 8.1
4.1	185	252	6.6	1.41	1.49	24.5 ± 2.9	0.0445 ± 15	0.25 ± 15	0.0408 ± 2.9	0.193	257.9 ± 7.5
5.1	201	255	7.01	1.31	0.12	24.64 ± 2.8	0.057 ± 4.4	0.319 ± 5.3	0.0406 ± 2.8	0.535	256.5 ± 7.1
5.2	310	273	11.3	0.91	1.18	23.95 ± 2.8	0.0485 ± 9.6	0.279 ± 10	0.0417 ± 2.8	0.284	263.6 ± 7.3
6.1	70	77	2.54	1.14	3.49	24.54 ± 4	0.068 ± 27	0.38 ± 28	0.0406 ± 4	0.146	257 ± 10
Sample 204025-4 (concordia age = 255 ± 2 Ma, MSWD (concordance) = 3.5, probability = 0.062)											
1.1	239	323	8.38	1.39	0.31	24.6 ± 1.1	0.0491 ± 4.6	0.275 ± 4.8	0.04065 ± 1.1	0.235	256.9 ± 2.8
2.1	1257	494	43.8	0.41	0.02	24.68 ± 0.76	0.05128 ± 1.5	0.2865 ± 1.7	0.04052 ± 0.76	0.461	256.1 ± 1.9
3.1	889	573	31.1	0.67	0.34	24.64 ± 0.94	0.0489 ± 3.1	0.2739 ± 3.3	0.04058 ± 0.94	0.287	256.4 ± 2.4
4.1	682	346	23.6	0.52	0.00	24.85 ± 0.85	0.0511 ± 2	0.2835 ± 2.2	0.04025 ± 0.85	0.384	254.4 ± 2.1
5.1	366	173	12.7	0.49	0.00	24.63 ± 0.99	0.0558 ± 5.5	0.312 ± 5.6	0.04059 ± 0.99	0.177	256.5 ± 2.5
6.1	134	79	4.63	0.61	0.00	24.9 ± 1.4	0.0519 ± 4.6	0.287 ± 4.8	0.04017 ± 1.4	0.287	253.9 ± 3.4
7.1	497	335	17.1	0.70	0.00	24.95 ± 0.91	0.0492 ± 2.5	0.2718 ± 2.6	0.04008 ± 0.91	0.346	253.4 ± 2.3
8.1	441	294	15.2	0.69	0.17	24.97 ± 0.95	0.0493 ± 3.1	0.2723 ± 3.3	0.04005 ± 0.95	0.290	253.1 ± 2.3
9.1	244	292	8.57	1.24	0.32	24.49 ± 1.1	0.048 ± 4.8	0.27 ± 4.9	0.04083 ± 1.1	0.230	258 ± 2.9
10.1	307	198	10.6	0.67	0.25	24.93 ± 1	0.0507 ± 3.9	0.28 ± 4	0.04011 ± 1	0.260	253.5 ± 2.6
Sample 204001 (concordia age = 252 ± 2 Ma, MSWD (concordance) = 0.099, probability = 0.75)											
1.1	509	412	17.2	0.84	–	25.44 ± 0.73	0.0531 ± 3.2	0.2877 ± 3.3	0.03931 ± 0.73	0.222	248.6 ± 1.8
2.1	106	166	3.62	1.61	0.00	25.27 ± 1.1	0.0495 ± 3.2	0.2701 ± 3.4	0.03956 ± 1.1	0.315	250.1 ± 2.6
3.1	130	102	4.51	0.81	1.15	24.99 ± 1.1	0.0586 ± 5.8	0.323 ± 5.9	0.04001 ± 1.1	0.185	252.9 ± 2.7
4.1	279	264	9.4	0.98	0.00	25.47 ± 0.85	0.0496 ± 2.2	0.2686 ± 2.4	0.03926 ± 0.85	0.355	248.2 ± 2.1
5.1	350	402	12	1.19	0.25	25.03 ± 0.78	0.0527 ± 2.7	0.2903 ± 2.8	0.03995 ± 0.78	0.283	252.5 ± 1.9
6.1	328	262	11	0.82	0.00	25.57 ± 0.77	0.0525 ± 1.9	0.2831 ± 2.1	0.0391 ± 0.77	0.375	247.3 ± 1.9

Table A3. Cont.

Spot No.	Content, ppm					Isotope ratios				Err. Corr.	Age (Ma) (1) ²⁰⁶ Pb/ ²³⁸ U (±%)
	U	Th	²⁰⁶ Pb*	²³² Th/ ²³⁸ U	% ²⁰⁶ Pb _c	(1) ²³⁸ U/ ²⁰⁶ Pb* (±%)	(1) ²⁰⁷ Pb*/ ²⁰⁶ Pb* (±%)	(1) ²⁰⁷ Pb*/ ²³⁵ U (±%)	(1) ²⁰⁶ Pb*/ ²³⁸ U (±%)		
7.1	158	137	5.41	0.90	0.00	25.07 ± 0.99	0.0525 ± 2.8	0.2888 ± 2.9	0.03989 ± 0.99	0.336	252.2 ± 2.5
8.1	1080	1337	37.2	1.28	0.12	25.01 ± 0.62	0.05114 ± 1.8	0.2819 ± 1.9	0.03999 ± 0.62	0.335	252.8 ± 1.5
9.1	177	187	6.03	1.09	0.27	25.34 ± 1	0.0537 ± 3.9	0.292 ± 4	0.03946 ± 1	0.250	249.5 ± 2.5
10.1	258	337	8.85	1.35	0.77	25.27 ± 0.91	0.0493 ± 4.7	0.269 ± 4.8	0.03956 ± 0.91	0.188	250.1 ± 2.2
10.1RE	422	911	14.6	2.23	0.43	24.97 ± 0.76	0.0499 ± 2.8	0.2757 ± 2.9	0.04004 ± 0.76	0.256	253.1 ± 1.9
9.1RE	247	281	8.73	1.18	3.35	25.1 ± 1.2	0.0503 ± 13	0.276 ± 13	0.03981 ± 1.2	0.093	251.6 ± 2.9

Note: errors in Standard calibration (not included in above errors but required when comparing data from different mounts) were: 0.84% (smp. 554), 0.23% (smp. 13103), 0.61% (smp. 204064 and smp. 204025-4), 0.53% (smp. 204001 and 18032), 0.62% (smp. 203004), 0.58% (smp. 203009), 0.57% (smp. 203025). Errors are 1-sigma. Pb_c and Pb* indicate the common and radiogenic portions, respectively. (1) Common Pb corrected using measured ²⁰⁴Pb. r—zircon rim, c—zircon core.

Appendix D

Table A4. Results of ⁴⁰Ar/³⁹Ar dating for samples 541-7 and 541-1.

T ⁰ C	t (min)	⁴⁰ Ar(STP)*	⁴⁰ Ar/ ³⁹ Ar	±1σ	³⁸ Ar/ ³⁹ Ar	±1σ	³⁷ Ar/ ³⁹ Ar	±1σ	³⁶ Ar/ ³⁹ Ar	±1σ	Ca/K	Σ ³⁹ Ar (%)	Age (Ma)±1σ	±1σ
Sample 541-7, amphibole, J** = 0.004126 ± 0.000045, Total fusion age = 259.6 ± 2.7 Ma (including J); Weighted Mean Plateau Age (800–1100 °C) = 259.3 ± 2.6 Ma (including J)														
400	10	58.8 × 10 ⁻⁹	962.202	23.376	0.6997	0.0347	301.4	302.4	3.0682	0.0776	538.0	0.1	372.3	42.7
500	10	52.3 × 10 ⁻⁹	97.486	0.356	0.0982	0.0035	23.8	23.9	0.2115	0.0032	42.5	1.4	243.3	6.4
600	10	113.2 × 10 ⁻⁹	82.677	0.197	0.0638	0.0011	35.9	19.6	0.1478	0.0013	64.0	4.7	269.3	3.6
650	10	75.6 × 10 ⁻⁹	61.450	0.114	0.0456	0.0013	31.7	19.5	0.0814	0.0019	56.6	7.6	258.9	4.5
700	10	70.6 × 10 ⁻⁹	62.033	0.101	0.0459	0.0026	11.2	11.3	0.0762	0.0019	20.1	10.3	272.4	4.5
750	10	81.7 × 10 ⁻⁹	69.017	0.148	0.0513	0.0018	10.8	10.8	0.1088	0.0020	19.3	13.1	255.4	4.6
800	10	70.3 × 10 ⁻⁹	56.862	0.228	0.0405	0.0020	10.3	8.7	0.0645	0.0014	18.5	16.1	261.6	3.9
850	10	89.2 × 10 ⁻⁹	51.503	0.095	0.0416	0.0013	20.6	17.7	0.0464	0.0013	36.9	20.2	261.4	3.7
900	10	104.1 × 10 ⁻⁹	45.611	0.077	0.0509	0.0006	14.5	12.5	0.0262	0.0006	25.9	25.6	261.9	2.9
950	10	270.3 × 10 ⁻⁹	42.614	0.035	0.0710	0.0003	18.1	4.0	0.0150	0.0004	32.2	40.7	263.9	2.7
975	10	344.4 × 10 ⁻⁹	40.258	0.059	0.0803	0.0003	3.8	3.0	0.0101	0.0002	6.7	61.0	258.1	2.6

Table A4. Cont.

T°C	t (min)	⁴⁰ Ar(STP)*	⁴⁰ Ar/ ³⁹ Ar	±1σ	³⁸ Ar/ ³⁹ Ar	±1σ	³⁷ Ar/ ³⁹ Ar	±1σ	³⁶ Ar/ ³⁹ Ar	±1σ	Ca/K	$\frac{\Sigma^{39}\text{Ar}}{(\%)}$	Age (Ma)±1σ	±1σ
1000	10	314.7 × 10 ⁻⁹	39.243	0.094	0.0826	0.0003	7.3	3.6	0.0088	0.0001	13.1	80.1	253.9	2.6
1025	10	141.1 × 10 ⁻⁹	41.104	0.051	0.0873	0.0008	7.7	7.7	0.0155	0.0008	13.7	88.3	253.3	3.0
1050	10	58.2 × 10 ⁻⁹	49.762	0.116	0.0952	0.0012	34.1	20.0	0.0404	0.0008	60.9	91.1	261.6	3.1
1075	10	42.4 × 10 ⁻⁹	55.232	0.310	0.1100	0.0028	64.8	46.4	0.0607	0.0021	115.8	92.9	258.3	5.0
1100	10	77.5 × 10 ⁻⁹	50.785	0.128	0.1101	0.0015	40.5	18.0	0.0439	0.0009	72.2	96.5	261.5	3.2
1125	10	51.0 × 10 ⁻⁹	58.458	0.163	0.1047	0.0017	15.6	15.6	0.0658	0.0023	27.8	98.6	269.2	5.2
1150	10	41.0 × 10 ⁻⁹	69.236	0.264	0.1167	0.0026	66.5	53.8	0.1009	0.0034	118.7	100.0	271.9	7.0
Sample 541-7, biotite, J = 0.004157 ± 0.000046, Total fusion age = 246.2 ± 2.6 Ma (including J); Weighted Mean Plateau Age (600–1100 °C) = 247.4 ± 2.6 Ma (including J)														
500	10	27.9 × 10 ⁻⁹	104.396	0.697	0.09468	0.00601	—	—	0.27652	0.00769	—	0.5	162.6	15.3
550	10	59.9 × 10 ⁻⁹	47.028	0.100	0.04206	0.00209	—	—	0.05581	0.00180	—	3.1	215.6	4.2
600	10	113.4 × 10 ⁻⁹	39.822	0.091	0.02789	0.00069	—	—	0.01589	0.00050	—	8.9	245.9	2.7
650	10	222.2 × 10 ⁻⁹	37.278	0.071	0.02627	0.00029	—	—	0.00696	0.00042	—	21.0	246.5	2.7
675	10	149.9 × 10 ⁻⁹	37.052	0.080	0.02597	0.00069	—	—	0.00509	0.00033	—	29.1	248.7	2.6
700	10	124.4 × 10 ⁻⁹	37.670	0.064	0.02695	0.00035	—	—	0.00786	0.00051	—	35.8	247.3	2.7
750	10	103.7 × 10 ⁻⁹	37.339	0.074	0.02692	0.00056	—	—	0.00641	0.00073	—	41.5	248.0	2.9
800	10	94.2 × 10 ⁻⁹	37.811	0.067	0.02879	0.00086	—	—	0.00953	0.00098	—	46.5	245.0	3.1
850	10	102.4 × 10 ⁻⁹	37.410	0.065	0.02597	0.00082	—	—	0.00611	0.00077	—	52.0	249.0	3.0
900	10	145.5 × 10 ⁻⁹	40.705	0.069	0.02919	0.00050	—	—	0.01825	0.00060	—	59.3	247.1	2.8
950	10	155.0 × 10 ⁻⁹	36.898	0.079	0.02597	0.00038	—	—	0.00536	0.00058	—	67.8	247.1	2.8
1000	10	210.6 × 10 ⁻⁹	36.715	0.120	0.02565	0.00045	—	—	0.00383	0.00033	—	79.4	248.9	2.7
1050	10	191.8 × 10 ⁻⁹	36.631	0.073	0.02563	0.00030	—	—	0.00410	0.00046	—	90.0	247.8	2.7
1100	10	181.9 × 10 ⁻⁹	36.872	0.056	0.02533	0.00035	—	—	0.00520	0.00035	—	100.0	247.3	2.6
Sample 541-1, amphibole, J = 0.004248 ± 0.000046, Total fusion age = 243.0 ± 2.5 Ma (including J); Weighted Mean Plateau Age (825–1150 °C) = 246.2 ± 2.6 Ma (including J)														
500	10	31.2 × 10 ⁻⁹	77.800	0.282	0.11220	0.00917	—	—	0.16738	0.01363	—	0.3	205.1	27.6
600	10	139.4 × 10 ⁻⁹	38.268	0.071	0.02827	0.00079	—	—	0.02005	0.00079	—	3.2	232.3	2.9
700	10	653.5 × 10 ⁻⁹	35.399	0.043	0.02317	0.00012	—	—	0.00899	0.00013	—	17.7	235.0	2.5
750	10	503.2 × 10 ⁻⁹	35.127	0.054	0.02288	0.00017	—	—	0.00695	0.00019	—	29.0	237.2	2.5
775	10	170.8 × 10 ⁻⁹	35.155	0.047	0.02277	0.00059	—	—	0.00767	0.00064	—	32.8	235.9	2.8
825	10	166.7 × 10 ⁻⁹	35.359	0.045	0.02399	0.00063	—	—	0.00489	0.00066	—	36.5	242.8	2.8
875	10	222.3 × 10 ⁻⁹	35.544	0.073	0.02524	0.00044	—	—	0.00491	0.00043	—	41.4	244.0	2.7

Table A4. Cont.

T ^o C	t (min)	⁴⁰ Ar(STP)*	⁴⁰ Ar/ ³⁹ Ar	±1σ	³⁸ Ar/ ³⁹ Ar	±1σ	³⁷ Ar/ ³⁹ Ar	±1σ	³⁶ Ar/ ³⁹ Ar	±1σ	Ca/K	$\frac{\sum^{39}\text{Ar}}{(\%)}$	Age (Ma)±1σ	±1σ
900	10	104.4 × 10 ⁻⁹	35.955	0.072	0.02671	0.00087	—	—	0.00668	0.00115	—	43.7	243.3	3.4
950	10	277.6 × 10 ⁻⁹	35.933	0.046	0.04623	0.00036	—	—	0.00552	0.00041	—	49.8	245.4	2.7
1000	10	563.7 × 10 ⁻⁹	36.239	0.064	0.06937	0.00019	—	—	0.00437	0.00017	—	62.0	249.7	2.6
1025	10	474.2 × 10 ⁻⁹	36.056	0.069	0.07438	0.00022	—	—	0.00454	0.00023	—	72.4	248.2	2.6
1050	10	461.0 × 10 ⁻⁹	35.568	0.053	0.07814	0.00022	—	—	0.00395	0.00023	—	82.6	246.1	2.6
1075	10	444.0 × 10 ⁻⁹	35.424	0.069	0.07900	0.00029	—	—	0.00399	0.00024	—	92.4	245.0	2.6
1100	10	232.3 × 10 ⁻⁹	35.886	0.059	0.05685	0.00044	—	—	0.00433	0.00046	—	97.5	247.5	2.7
1150	10	98.3 × 10 ⁻⁹	37.409	0.070	0.07940	0.00100	—	—	0.00793	0.00110	—	99.6	250.5	3.4
1200	10	26.4 × 10 ⁻⁹	50.260	0.305	0.13225	0.00578	—	—	0.04933	0.00557	—	100.0	254.6	11.3
Sample 541-1, biotite, J = 0.004197 ± 0.000046, Total fusion age, = 244.4 ± 2.5 Ma (including J); Weighted Mean Plateau Age (600–1100 °C) = 245.1 ± 2.6 Ma (including J)														
500	10	24.7 × 10 ⁻⁹	62.858	0.481	0.05824	0.00526	—	—	0.13266	0.00546	—	0.6	170.8	11.4
550	10	61.8 × 10 ⁻⁹	42.346	0.082	0.02759	0.00059	—	—	0.03724	0.00134	—	2.7	222.9	3.5
600	10	98.5 × 10 ⁻⁹	38.331	0.079	0.02335	0.00087	—	—	0.01205	0.00063	—	6.3	245.8	2.8
625	10	131.7 × 10 ⁻⁹	37.485	0.069	0.02395	0.00054	—	—	0.01029	0.00029	—	11.4	243.6	2.6
650	10	221.0 × 10 ⁻⁹	36.479	0.069	0.02346	0.00043	—	—	0.00522	0.00032	—	20.0	246.9	2.6
675	10	176.7 × 10 ⁻⁹	36.356	0.054	0.02358	0.00038	—	—	0.00495	0.00049	—	27.0	246.6	2.7
700	10	194.7 × 10 ⁻⁹	36.809	0.060	0.02346	0.00034	—	—	0.00695	0.00030	—	34.6	245.6	2.6
725	10	155.0 × 10 ⁻⁹	36.236	0.063	0.02306	0.00032	—	—	0.00567	0.00050	—	40.7	244.4	2.7
750	10	108.4 × 10 ⁻⁹	36.687	0.065	0.02407	0.00069	—	—	0.00657	0.00078	—	44.9	245.6	3.0
800	10	103.5 × 10 ⁻⁹	37.210	0.082	0.02545	0.00060	—	—	0.00886	0.00096	—	48.9	244.6	3.2
850	10	115.0 × 10 ⁻⁹	36.905	0.113	0.02457	0.00073	—	—	0.00925	0.00065	—	53.4	241.8	2.9
900	10	145.6 × 10 ⁻⁹	36.700	0.080	0.02404	0.00063	—	—	0.00775	0.00070	—	59.0	243.4	2.9
950	10	194.8 × 10 ⁻⁹	36.070	0.056	0.02409	0.00048	—	—	0.00537	0.00036	—	66.8	243.9	2.6
1000	10	317.4 × 10 ⁻⁹	36.108	0.054	0.02420	0.00021	—	—	0.00487	0.00020	—	79.4	245.1	2.6
1050	10	302.7 × 10 ⁻⁹	36.324	0.085	0.02543	0.00031	—	—	0.00525	0.00028	—	91.3	245.8	2.6
1100	10	225.3 × 10 ⁻⁹	37.033	0.076	0.02326	0.00030	—	—	0.00679	0.00030	—	100.0	247.4	2.6

Note: * volume of argon in cm³ occupied under normal conditions, ** parameter characterizing the neutron flux intensity.

References

1. Obruchev, V.A. Precambrian of the Taimyr Krai and Severnaya Zemlya. In *The Stratigraphy of the USSR*; Arkhangelsky, A.D., Ed.; Publishing House of the AS USSR: Moscow-Leningrad, Russia, 1939; Volume 1, pp. 493–501. (In Russian)
2. Urvantsev, N.N. The Taimyr foldbelt. *Bull. Norilsk Kombinat.* **1949**, *1*, 4–12. (In Russian)
3. Ravich, M.G. The Precambrian of Taimyr. In *Proceedings of the Institute of Arctic Geology (NIIGA)*; Korzhinsky, D.S., Obruchev, S.V., Eds.; Vodtransizdat: Moscow-Leningrad, Russia, 1954; Volume 76, p. 311. (In Russian)
4. Daminova, A.M. Age of the complex of crystalline schists of the Taimyr Peninsula. *Sov. Geol.* **1957**, *58*, 50–55. (In Russian)
5. Egiazarov, B.K. Geology of the Severnaya Zemlya archipelago. In *Proceedings of the Institute of Arctic Geology (NIIGA)*; Lobanov, M.F., Ed.; Gostoptekhizdat: Leningrad, Russia, 1959; Volume 94, p. 137. (In Russian)
6. Vakar, V.A. The trap formations of Taimyr. In *Petrography of Eastern Siberia*; Afanasiev, G.D., Ed.; AS USSR: Moscow, Russia, 1962; pp. 256–340. (In Russian)
7. Pogrebitsky, Y.E. *Paleotectonic Analysis of the Taimyr Fold System*; Nedra: Leningrad, Russia, 1971; p. 248. (In Russian)
8. Zabayaka, A.I. Stratigraphy and sedimentary formations of the Precambrian of north-western Taimyr. In *Proceedings of SNIIGGIMS*; Krasnoyarskoye Knizhnoye Izdatelstvo: Krasnoyarsk, Russia, 1974; p. 126. (In Russian)
9. Makhlaev, L.V. The Taimyr folded area. In *The Precambrian of Continents. Folded Areas and Young Platforms of Eastern Europe and Asia*; Bogolepov, K.V., Votakh, O.A., Eds.; Nauka: Novosibirsk, Russia, 1978; pp. 147–168. (In Russian)
10. Bezzubtsev, V.V.; Zalyalyaev, P.S.; Sakovich, A.B. *Geological Map of Mountainous Taimyr, Scale 1:500,000; Explanatory Note*; Krasnoyarskgeologiya: Krasnoyarsk, Russia, 1986; p. 177. (In Russian)
11. Zabayaka, A.I.; Zabayaka, I.D.; Vernikovskiy, V.A.; Serdyuk, S.S.; Zlobin, M.M. *Geological Structure and Tectonic Evolution of Northeastern Taimyr*; Nauka: Novosibirsk, Russia, 1986; p. 144. (In Russian)
12. Uflyand, A.K.; Natapov, L.M.; Lopatin, V.M.; Chernov, D.V. Concerning the tectonic nature of Taimyr. *Geotectonika* **1991**, *6*, 76–93. (In Russian)
13. Vernikovskiy, V.A. *Geodynamic Evolution of Taimyr Folded Area*; Publishing House SB RAS SPC UIGGM: Novosibirsk, Russia, 1996; p. 202. (In Russian)
14. Bogdanov, N.A.; Khain, V.E.; Rosen, O.M.; Shipilov, E.V.; Vernikovskiy, V.A.; Drachev, S.L.; Kostyuchenko, S.H.; Kuzmichev, A.B.; Sekretov, S.B. *Tectonic Map of the Kara and Laptev Seas and North Siberia (Scale 1:2,500,000)*; Explanatory note; Kartografiya: Moscow, Russia, 1998; p. 127. (In Russian)
15. Khain, V.E. *Tectonics of Continents and Oceans (Year 2000)*; Scientific World Publishing House: Moscow, Russia, 2001; p. 606. (In Russian)
16. Zonenshain, L.P.; Natapov, L.M. Tectonic history of Arctic. In *Actual Problems of Continent and Ocean Tectonics*; Yanshin, A.L., Ed.; Nauka: Moscow, Russia, 1987; pp. 31–57. (In Russian)
17. Zonenshain, L.P.; Kuzmin, M.I.; Natapov, L.M. *Geology of the USSR: A Plate Tectonic Synthesis*; Page, B.M., Ed.; Geodynamic Series, 21; American Geophysical Union: Washington, DC, USA, 1990; p. 242.
18. Golonka, J.; Bocharova, N.Y.; Ford, D.; Edrich, M.E.; Bednarczyk, J.; Wildharber, J. Paleogeographic reconstructions and basins development of the Arctic. *Mar. Pet. Geol.* **2003**, *20*, 211–248. [[CrossRef](#)]
19. Metelkin, D.V.; Kazansky, A.Y.; Vernikovskiy, V.A.; Gee, D.G.; Torsvik, T. First paleomagnetic data for the early Paleozoic of the Severnaya Zemlya archipelago and their geodynamic interpretation. *Rus. Geol. Geophys.* **2000**, *41*, 1816–1820.
20. Metelkin, D.V.; Vernikovskiy, V.A.; Kazansky, A.Y.; Bogolepova, O.K.; Gubanov, A.P. Paleozoic history of the Kara microcontinent and its relation to Siberia and Baltica: Paleomagnetism, paleogeography and tectonics. *Tectonophysics* **2005**, *398*, 225–243. [[CrossRef](#)]
21. Metelkin, D.V.; Vernikovskiy, V.A.; Kazansky, A.Y. Neoproterozoic evolution of Rodinia: Constraints from new paleomagnetic data on the western margin of the Siberian craton. *Rus. Geol. Geophys.* **2007**, *48*, 32–45. [[CrossRef](#)]
22. Metelkin, D.V.; Vernikovskiy, V.A.; Matushkin, N.Y. Arctida between Rodinia and Pangea. *Precam. Res.* **2015**, *259*, 114–129. [[CrossRef](#)]

23. Gee, D.G.; Bogolepova, O.K.; Lorenz, H. The Timanide, Caledonide and Uralide orogens in the Eurasian high Arctic, and relationships to the palaeocontinents Laurentia, Baltica and Siberia. In *European Lithosphere Dynamics. Geological Society London, Memoirs*; Gee, D.G., Stephenson, R.A., Eds.; Geological Society of London: London, UK, 2006; Volume 32, pp. 507–520. [[CrossRef](#)]
24. Li, Z.X.; Bogdanova, S.V.; Collins, A.S.; Davidson, A.; De Waele, B.; Ernst, R.E.; Fitzsimons, I.C.W.; Fuck, R.A.; Gladkochub, D.P.; Jacobs, J.; et al. Assembly, configuration, and break-up history of Rodinia: A synthesis. *Precam. Res.* **2008**, *160*, 179–210. [[CrossRef](#)]
25. Lorenz, H.; Männik, P.; Gee, D.; Proskurnin, V. Geology of the Severnaya Zemlya Archipelago and the North Kara Terrane in the Russian high Arctic. *Int. J. Earth Sci.* **2008**, *97*, 519–547. [[CrossRef](#)]
26. Pisarevsky, S.A.; Natapov, L.M.; Donskaya, T.V.; Gladkochub, D.P.; Vernikovskiy, V.A. Proterozoic Siberia: A promontory of Rodinia. *Precam. Res.* **2008**, *160*, 66–76. [[CrossRef](#)]
27. Pease, V.; Scott, R.A. Crustal affinities in the Arctic Uralides, northern Russia: Significance of detrital zircon ages from Neoproterozoic and Palaeozoic sediments in Novaya Zemlya and Taimyr. *J. Geol. Soc.* **2009**, *166*, 517–527. [[CrossRef](#)]
28. Drachev, S.S. Fold belts and sedimentary basins of the Eurasian Arctic. *Arktos* **2016**, *2*, 21. [[CrossRef](#)]
29. Shipilov, E.V.; Vernikovskiy, V.A. The Svalbard-Kara plates junction: Structure and geodynamic history. *Rus. Geol. Geophys.* **2010**, *51*, 58–71. [[CrossRef](#)]
30. Lawver, L.A.; Ganagan, L.M.; Norton, I. Paleogeographic and tectonic evolution of the Arctic region during the Paleozoic. In *Arctic Petroleum Geology. Geological Society London, Memoirs*; Spencer, A.M., Embry, A.F., Gautier, D.L., Stoupakova, A.V., Sørensen, K., Eds.; Geological Society of London: London, UK, 2011; Volume 35, pp. 61–77. [[CrossRef](#)]
31. Vernikovskiy, V.A.; Dobretsov, N.L.; Metelkin, D.V.; Matushkin, N.Y.; Koulakov, I.Y. Concerning tectonics and the tectonic evolution of the Arctic. *Rus. Geol. Geophys.* **2013**, *54*, 838–858. [[CrossRef](#)]
32. Vernikovskiy, V.A. Neoproterozoic and Late Paleozoic Taimyr Orogenic and Ophiolitic belts, North Asia: A review and models for their formation. In *The Proceedings of the 30th International Geological Congress*; Liu, G., Ed.; VSP: Utrecht, The Netherlands, 1997; Volume 7, pp. 121–138.
33. Vernikovskiy, V.A.; Vernikovskaya, A.E. Central Taimyr accretionary belt (Arctic Asia): Meso-Neoproterozoic tectonic evolution and Rodinia break up. *Precam. Res.* **2001**, *110*, 127–141. [[CrossRef](#)]
34. Vernikovskiy, V.A.; Pease, V.L.; Vernikovskaya, A.E.; Romanov, A.P.; Gee, D.G.; Travin, A.V. First report of early Triassic A-type granite and syenite intrusions from Taimyr: Product of the northern Eurasian superplume? *Lithos* **2003**, *66*, 23–36. [[CrossRef](#)]
35. Vernikovskiy, V.; Shemin, G.; Deev, E.; Metelkin, D.; Matushkin, N.; Pervukhina, N. Geodynamics and oil and gas potential of the Yenisei-Khatanga basin (Polar Siberia). *Minerals* **2018**, *8*, 510. [[CrossRef](#)]
36. Zolotukhin, V.V.; Al'mukhamedov, A.I. Traps of the Siberian platform. In *Continental Flood Basalts*; Macdougall, J.D., Ed.; Kluwer Academic Publishers: Dordrecht, The Netherlands, 1988; pp. 273–310.
37. Zolotukhin, V.V. *Particularities of the Tulay-Kiryak Differentiated intrusion on Taimyr*; Nauka: Novosibirsk, Russia, 1990; p. 111.
38. Renne, P.R.; Basu, A.R. Rapid eruption of the Siberian Traps flood basalts at the Permo–Triassic Boundary. *Science* **1991**, *253*, 176–179. [[CrossRef](#)]
39. Campbell, I.H.; Czamanske, G.K.; Fedorenko, V.A.; Hill, R.I.; Stepanov, V. Synchronism of the Siberian Traps and the Permian-Triassic Boundary. *Science* **1992**, *258*, 1760–1763. [[CrossRef](#)]
40. Sharma, M. Siberian traps. In *Large Igneous Provinces: Continental, Oceanic, and Planetary Flood Volcanism, Geophysical Monograph*; Mahoney, J.J., Coffin, M.F., Eds.; American Geophysical Union: Washington, DC, USA, 1997; Volume 100, pp. 273–295. [[CrossRef](#)]
41. Vasiljev, Y.R.; Zolotukhin, V.V.; Feoktistov, G.D.; Prusskaya, S.N. Volume estimation and genesis of Permian-Triassic trap magmatism from Siberian platform. *Rus. Geol. Geophys.* **2000**, *41*, 1696–1705.
42. Dobretsov, N.L.; Vernikovskiy, V.A. Mantle plumes and their geological manifestations. *Int. Geol. Rev.* **2001**, *43*, 771–787. [[CrossRef](#)]
43. Vernikovskiy, V.A.; Pease, V.L.; Vernikovskaya, A.E.; Romanov, A.P.; Gee, D.J.; Travin, A.V. Early Triassic A-granites in the Taimyr region as a result of a North Asian superplume. *Dokl. Earth Sci.* **2001**, *380*, 758–763.
44. Kamo, S.L.; Czamanske, G.K.; Amelin, Y.; Fedorenko, V.A.; Davis, D.W.; Trofimov, V.R. Rapid eruption of Siberian flood-volcanic rocks and evidence for coincidence with the Permian–Triassic boundary and mass extinction at 251 Ma. *Earth Plan. Sci. Lett.* **2003**, *214*, 75–91. [[CrossRef](#)]

45. Augland, L.E.; Ryabov, V.V.; Vernikovskiy, V.A.; Planke, S.; Polozov, A.G.; Callegaro, S.; Jerram, D.A.; Svensen, H.H. The main pulse of the Siberian Traps expanded in size and composition. *Sci. Rep.* **2019**, *9*, 18723. [[CrossRef](#)]
46. Ravich, M.G.; Chaika, L.A. Differentiated intrusion of trapp formation from Taimyr folded area. *Izv. AN SSSR Ser. Geol.* **1956**, *1*, 50–64. (In Russian)
47. Ravich, M.G.; Chayka, L.A. Small intrusions of the Byrranga Ridge (Taimyr Pen). In *Proceedings of the Institute of Arctic Geology (NIIGA)*; NIIGA: Leningrad, Russia, 1959; Volume 88, p. 147. (In Russian)
48. Ravich, M.G.; Chayka, L.A. Metamorphic and magmatic formations of the Precambrian of Taimyr. In *Petrography of Eastern Siberia*; Publishing house of AS USSR: Moscow, Russia, 1962; Volume 2, pp. 590–719. (In Russian)
49. Makhlaev, L.V.; Korobova, N.I. *Genetic Granitoid Series of the Precambrian of Taimyr*; Krasnoyarskoye knizhnoye izdatelstvo: Krasnoyarsk, Russia, 1972; p. 130. (In Russian)
50. Vernikovskiy, V.A.; Neimark, L.A.; Ponomarchuk, V.A.; Vernikovskaya, A.E.; Kireev, A.D.; Kuzmin, D.S. Geochemistry and age of collisional granitoids and metamorphites of the Kara microcontinent (Northern Taimyr). *Rus. Geol. Geophys.* **1995**, *36*, 46–60.
51. Pease, V.L.; Kuzmichev, A.B.; Danukalova, M.K. The New Siberian Islands and evidence for the continuation of the Uralides, Arctic Russia. *J. Geol. Soc.* **2015**, *172*, 1–4. [[CrossRef](#)]
52. Kurapov, M.Y.; Ershova, V.B.; Makariev, A.A.; Makarieva, E.V.; Khudoley, A.K.; Luchitskaya, M.V.; Prokopiev, A.V. Carboniferous granitoid magmatism of Northern Taimyr: Results of isotopic-geochemical study and geodynamic interpretation. *Geotectonics* **2018**, *52*, 225–239. [[CrossRef](#)]
53. Khudoley, A.K.; Verzhbitsky, V.E.; Zastrozhnov, D.A.; O’Sullivan, P.; Ershova, V.B.; Proskurnin, V.F.; Tuchkova, M.I.; Rogov, M.A.; Kyser, T.K.; Malyshev, S.V.; et al. Late Paleozoic—Mesozoic tectonic evolution of the Eastern Taimyr-Severnaya Zemlya Fold and Thrust Belt and adjoining Yenisey-Khatanga Depression. *J. Geodynam.* **2018**, *119*, 221–241. [[CrossRef](#)]
54. Vernikovskiy, V.A.; Sal’nikova, E.B.; Kotov, A.B.; Ponomarchuk, V.A.; Kovach, V.P.; Travin, A.V.; Yakovleva, S.Z.; Berezhnaya, N.G. Age of post-collisional granitoids, North Taimyr: U-Pb, Sm-Nd, Rb-Sr and Ar-Ar data. *Dokl. Earth Sci.* **1998**, *363A*, 1191–1194.
55. Vernikovskiy, V.A.; Vernikovskaya, A.E.; Kovach, V.P.; Kotov, A.B.; Sal’nikova, E.B. Sources of granitoids and the evolutionary stages of the continental crust in the Taimyr folded area. *Geochem. Int.* **1999**, *37*, 493–502.
56. Proskurnina, M.A.; Proskurnin, V.F.; Remizov, D.N.; Larionov, A.N. Ring intrusions of the Bepamyatnaya Areal: Manifestations of shoshonite-latitude magmatism in Northern Taimyr. *Reg. Geol. Met.* **2019**, *79*, 5–22. (In Russian)
57. Dewey, J.F.; Holdsworth, R.E.; Strachan, R.A. Transpression and transtension zones. *Geol. Soc. Spec. Publ.* **1998**, *135*, 1–14. [[CrossRef](#)]
58. Korikovskiy, S.P. Contrasting models of prograde-retrograde evolution of metamorphism of Phanerozoic fold belts in collision and subduction zones. *Petrography* **1995**, *3*, 45–63. (In Russian)
59. Condie, K.C. *Plate Tectonics and Crustal Evolution*, 4th ed.; Butterworth Heinemann. Bookcraft (Bath) Ltd.: Oxford, UK, 1997; p. 287.
60. Dewey, J.F. Extensional collapse of orogens. *Tectonics* **1988**, *7*, 1123–1139. [[CrossRef](#)]
61. Gerdes, A.; Wörner, G.; Henk, A. Post-collisional granite generation and HT-LP metamorphism by radiogenic heating: The Variscan South Bohemian Batholith. *J. Geol. Soc.* **2000**, *157*, 577–587. [[CrossRef](#)]
62. Maltsev, Y.M.; Bezzubtsev, V.V. Concerning thrust structures of the Taimyr folded area. *Geol. Geofiz.* **1979**, *3*, 47–54. (In Russian)
63. Inger, S.; Scott, R.A.; Golionko, B. Tectonic evolution of the Taimyr Peninsula, northern Russia: Implications for Arctic continental assembly. *J. Geol. Soc.* **1999**, *156*, 1069–1072. [[CrossRef](#)]
64. Badanina, I.Y.; Malitch, K.N.; Romanov, A.P. Isotopic-geochemical characteristics of the ore-bearing ultramafic-mafic intrusions of western Taimyr, Russia. *Dokl. Earth Sci.* **2014**, *458*, 1165–1167. [[CrossRef](#)]
65. Makhlaev, L.V. Tectonic nature of the Mamont-Shrenk block (Central Taimyr). *Izv. An. SSSR. Geol.* **1988**, *4*, 77–87. (In Russian)
66. Vernikovskiy, V.A.; Neimark, L.A.; Ponomarchuk, V.A.; Yakovleva, S.Z. New U-Pb, Sm-Nd, Rb-Sr, and K-Ar ages for the North Taimyr collisional granites and metamorphites. *Dokl. Earth Sci.* **1996**, *345A*, 329–334.

67. Vernikovskiy, V.A.; Metelkin, D.V.; Vernikovskaya, A.E.; Sal'nikova, E.B.; Kovach, V.P.; Kotov, A.B. The oldest island arc complex of Taimyr: Concerning the issue of the Central-Taimyr accretionary belt formation and paleogeodynamic reconstructions in the arctic. *Dokl. Earth Sci.* **2011**, *436*, 186–192. [[CrossRef](#)]
68. Pease, V.; Gee, D.G.; Vernikovskiy, V.; Vernikovskaya, A.; Kireev, S. Geochronological evidence for late-Grenvillian magmatic and metamorphic events in central Taimyr, northern Siberia. *Terra Nova* **2001**, *13*, 270–280. [[CrossRef](#)]
69. Vernikovskiy, V.A.; Kotov, A.B.; Ponomarchuk, V.A.; Salnikova, E.B.; Kovach, V.P.; Travin, A.V. A Late Riphean—Vendian event in the formation of Northern Taimyr. *Dokl. RAN* **1997**, *352*, 218–221. (In Russian)
70. Zakharov, Y.I.; Ravich, M.G.; Shulyatin, O.G. Metamorphic facies of the Taimyr folded area. In *Metamorphic Complexes of Asia*; Sobolev, V.S., Lepezin, G.G., Dobretsov, N.L., Eds.; Nauka: Novosibirsk, Russia, 1977; Volume 365, pp. 164–176. (In Russian)
71. Demina, L.I.; Belov, V.P. Metamorphic zoning of the Precambrian of Northwestern Taimyr. *Bull. MOIP Geol. Sec.* **1979**, *54*, 55–66. (In Russian)
72. Vernikovskiy, V.A.; Zabiya, I.D. Metamorphic complexes of Northeastern Taimyr. *Geol. Geofiz.* **1985**, *7*, 57–64. (In Russian)
73. Vernikovskiy, V.A. Metamorphic formations and geodynamics of the Northern Taimyr. *Rus. Geol. Geophys.* **1992**, *33*, 42–49.
74. Vernikovskiy, V.A. Particularities of formation of metamorphic complexes of Northern Taimyr in the Riphean and Paleozoic. *Petrology* **1995**, *3*, 63–81.
75. Kaban'kov, V.Y.; Sobolevskaya, R.F. Late Precambrian—Early Paleozoic stage of geological development of Taimyr–North Land folded area. In *Tectonics of Baikal (Riphean) Megacomplex of Siberia*; Bogolepov, K.V., Basharin, A.K., Eds.; Publishing house of IGG SB AS USSR: Novosibirsk, Russia, 1981; pp. 55–62. (In Russian)
76. Proskurnin, V.F. Magmatic formations of the Taimyr-Severnaya Zemlya folded system, their ore potential and geodynamic formation particularities. In *Ore Potential of Magmatic Formations of Siberia*; SNIIGGIMS: Novosibirsk, Russia, 1991; pp. 33–39. (In Russian)
77. Makar'ev, A.A.; Lazarenko, N.P.; Rogozov, Y.G. New data on Cambrian deposits from North Land Archipelago. In *Lithology and Paleogeography of the Barents and Kara Seas*; Sorokov, D.S., Kulakov, Y.N., Eds.; NIIGA Publishing House: Leningrad, Russia, 1981; pp. 97–109. (In Russian)
78. Matukhin, R.G.; Menner, V.V. *Stratigraphy Silurian and Devonian Strata of Severnaya Zemlya*; SNIIGGIMS: Novosibirsk, Russia, 1999; p. 174. (In Russian)
79. Bogolepova, O.K.; Gubanov, A.P.; Raevskaya, E.G. The Cambrian of the Severnaya Zemlya Archipelago, Russia. *Newsl. Stratig.* **2001**, *39*, 73–91. [[CrossRef](#)]
80. Kartseva, G.N.; Lopatin, B.G.; Orlov, V.P.; Pogrebitsky, Y.E. *State Geological Map of the Russian Federation (New Series), Scale 1:1,000,000, Sheet S-47-49*; VSEGEI Cartographic factory: St. Petersburg, Russia, 1998. (In Russian)
81. Nagaitseva, N.N.; Lopatin, V.G. *State Geological Map of the Russian Federation (New Series), Scale 1:1,000,000, Sheet T-44-46*; VSEGEI Cartographic factory: St. Petersburg, Russia, 2000. (In Russian)
82. Markovskiy, V.A.; Shneider, G.V.; Proskurnin, V.F.; Kaban'kov, V.Y.; Sobolevskaya, R.F.; Lopatin, B.G. *State Geological Map of the Russian Federation (New Series), Scale 1:1,000,000, Sheet T-48-50*; VSEGEI Cartographic factory: St. Petersburg, Russia, 2003. (In Russian)
83. Makaryev, A.A.; Makaryeva, E.M. *State Geological Map of the Russian Federation (Third Generation), Scale 1:1,000,000, Sheet T-45-48*; Polar Marine Geosurvey Expedition Stock Venture: Saint Petersburg, Russia, 2011. (In Russian)
84. Proskurnin, V.F.; Shneider, G.V.; Gavrish, A.V.; Nagaitseva, N.N.; Romanov, A.P.; Gromov, P.A.; Proskurnina, M.A.; Mokhov, V.V.; Nelyubin, V.V.; Lokhov, D.K.; et al. *State Geological Map of the Russian Federation. Scale 1:1,000,000. (Third Generation) Series Taimyr—Severnaya Zemlya. Sheet S-46—Tareya. Explanatory Note*; VSEGEI Cartographic factory: St. Petersburg, Russia, 2016; p. 586. (In Russian)
85. Malitch, N.S. *State Geological Map of the Russian Federation. Scale 1:200,000. Series—Taimyr. Explanatory Note*; Sevmorgeologiya: Moscow, Russia, 2000; p. 186. (In Russian)
86. Zabiya, A.I.; Vernikovskiy, V.A.; Zabiya, I.D.; Zlobin, M.I.; Korobeinikov, A.F.; Serduk, S.S. Geochemical model of gold distribution in the exocontact rim of a granitoid pluton. *Dokl. Akad. Nauk* **1990**, *313*, 959–962. (In Russian)

87. Malitch, K.N.; Lokhov, D.K.; Proskurnin, V.F.; Puchkov, V.N.; Badanina, I.Y.; Chervyakovskaya, M.A. U-Pb and Lu-Hf isotopes in rocks of the Dyumtaley ore-bearing intrusion (Taimyr, Russia): New evidence for the role of the depleted mantle in its genesis. *Dokl. Earth Sci.* **2020**, *492*, 1–5.
88. Makhlaev, L.V. *The Isolithogenic Granitoid Series*; Nauka: Novosibirsk, Russia, 1987; p. 153. (In Russian)
89. Proskurnin, V.F.; Sal'nikov, V.I. Magmatogenic-metamorphogenic-hydrothermal zoning of the Chukotka-Olenkin region (Taimyr Peninsula). *Geol. Ore Dep.* **1990**, *32*, 91–95. (In Russian)
90. Black, L.P.; Kamo, S.L.; Allen, C.M.; Aleinikoff, J.N.; Davis, D.W.; Korsch, R.J.; Foudoulis, C. TEMORA 1: A new zircon standard for Phanerozoic U-Pb geochronology. *Chem. Geol.* **2003**, *200*, 155–170. [[CrossRef](#)]
91. Wiedenbeck, M.; Allé, P.; Corfu, F.; Griffin, W.L.; Meier, M.; Oberli, F.; von Quadt, A.; Roddick, J.C.; Spiegel, W. Three natural zircon standards for U-Th-Pb, Lu-Hf, trace element and REE analyses. *Geostand. Newslet.* **1995**, *19*, 1–23. [[CrossRef](#)]
92. Larionov, A.N.; Andreichev, V.A.; Gee, D.G. The Vendian alkaline igneous suite of northern Timan: Ion microprobe U–Pb zircon ages of gabbros and syenite. In *The Neoproterozoic Timanide Orogen of Eastern Baltica*, 1st ed.; Gee, D.G., Pease, V.L., Eds.; Geology. Society, London, Memoirs: London, UK, 2004; Volume 30, pp. 69–74. [[CrossRef](#)]
93. Ludwig, K.R. *SQUID 1.12 A User's Manual. A Geochronological Toolkit for Microsoft Excel*, 1st ed.; Berkeley Geochronology Center Special Publication: Berkeley, CA, USA, 2005; p. 22. Available online: http://bgc.org/isoplot_etc/squid/SQUID2_5Manual.pdf (accessed on 25 June 2020).
94. Ludwig, K.R. *User's Manual for ISOPLOT/Ex 3.22. A Geochronological Toolkit for Microsoft Excel*, 1st ed.; Berkeley Geochronology Center Special Publication: Berkeley, CA, USA, 2005; p. 71. Available online: http://www.bgc.org/isoplot_etc/isoplot/Isoplot3_75-4_15manual.pdf (accessed on 25 June 2020).
95. Stacey, J.S.; Kramers, J.D. Approximation of terrestrial lead isotope evolution by a two-stage model. *Earth Planet Sci. Lett.* **1975**, *26*, 207–221. [[CrossRef](#)]
96. Travin, A.V.; Yudin, D.S.; Vladimirov, A.G.; Khromykh, S.V.; Volkova, N.I.; Mekhonoshin, A.S.; Kolotilina, T.B. Thermochronology of the Chernorud granulite zone, Ol'khon Region, Western Baikal area. *Geochem. Int.* **2009**, *47*, 1107–1124. [[CrossRef](#)]
97. Middlemost, E.A.K. Naming materials in the magma/igneous rock system. *Earth Sci. Rev.* **1994**, *37*, 215–224. [[CrossRef](#)]
98. Frost, B.R.; Barnes, C.G.; Collins, W.J.; Arculus, R.J.; Ellis, D.J.; Frost, C.D. A Geochemical Classification for Granitic Rocks. *J. Petrol.* **2001**, *42*, 2033–2048. [[CrossRef](#)]
99. Maniar, P.D.; Piccoli, P.M. Tectonic discrimination of granitoids. *Geol. Soc. Am. Bull.* **1989**, *101*, 635–643. [[CrossRef](#)]
100. Rudnick, R.L.; Gao, S. The Composition of the Continental Crust. In *Treatise on Geochemistry, The Crust*, 1st. Ed.; Holland, H.D., Turekian, K.K., Eds.; Elsevier-Pergamon: Oxford, UK, 2003; Volume 3, pp. 1–64. [[CrossRef](#)]
101. Evensen, N.M.; Hamilton, P.J.; O'Nions, R.K. Rare-earth abundances in chondritic meteorites. *Geochim. Cosmochim. Acta* **1978**, *42*, 1199–1212. [[CrossRef](#)]
102. McDonough, W.F.; Sun, S.-S. The composition of the Earth. *Chem. Geol.* **1995**, *120*, 223–254. [[CrossRef](#)]
103. Batchelor, R.A.; Bowden, P. Petrogenetic interpretation of granitoid rocks series using multicationic parameters. *Chem. Geol.* **1985**, *48*, 43–55. [[CrossRef](#)]
104. Mason, R. *Petrology of the Metamorphic Rocks*; George Allen & Unwin: London, UK, 1978; p. 254.
105. Pearce, J.A.; Harris, N.B.W.; Tindle, A.G. Trace element discrimination diagrams for the tectonic interpretation of granitic rocks. *J. Petrol.* **1984**, *25*, 956–983. [[CrossRef](#)]
106. Pearce, J.A. Sources and settings of granitic rocks. *Episodes* **1996**, *19*, 120–125. [[CrossRef](#)]
107. Vernikovskaya, A.E.; Vernikovskiy, V.A.; Matushkin, N.Y.; Romanova, I.V.; Berejnaya, N.G.; Larionov, A.N.; Travin, A.V. Middle Paleozoic and Early Mesozoic anorogenic magmatism of the South Yenisei Ridge: First geochemical and geochronological data. *Rus. Geol. Geophys.* **2010**, *51*, 548–562. [[CrossRef](#)]
108. Lorenz, H.; Gee, D.G.; Whitehouse, M.J. New geochronological data on Palaeozoic igneous activity and deformation in the Severnaya Zemlya Archipelago, Russia, and implications for the development of the Eurasian Arctic margin. *Geol. Mag.* **2007**, *144*, 105–125. [[CrossRef](#)]

109. Zhang, X.; Pease, V.; Skogseid, J.; Wohlgemuth-Ueberwasser, C. Reconstruction of tectonic events on the northern Eurasia margin of the Arctic, from U-Pb detrital zircon provenance investigations of late Paleozoic to Mesozoic sandstones in southern Taimyr Peninsula. *Geol. Soc. Am. Bull.* **2016**, *128*, 29–46. [[CrossRef](#)]
110. Priyatkina, N.; Collins, W.J.; Khudoley, A.; Zastrozhnov, D.; Ershova, V.; Chambarlain, K.; Shatsillo, A.; Proskurnin, V. The Proterozoic evolution of northern Siberian Craton margin: A comparison of U-Pb-Hf signatures from sedimentary units of the Taimyr orogenic belt and the Siberian platform. *Int. Geol. Rev.* **2017**, *59*, 1632–1656. [[CrossRef](#)]
111. Ershova, V.; Anfinson, O.; Prokopiev, A.; Khudoley, A.; Stockli, D.; Faleide, J.-I.; Gaina, C.; Malyshev, N. Detrital Zircon (U-Th)/He Ages from Paleozoic Strata of the Severnaya Zemlya Archipelago: Deciphering Multiple Episodes of Paleozoic Tectonic Evolution within the Russian High Arctic. *J. Geodyn.* **2018**, *119*, 210–220. [[CrossRef](#)]
112. Pease, V.; Lane, L.; Faleide, J.I.; Stephenson, R.; Coakley, B. Scientific network to decipher crustal evolution of the Arctic. *EOS* **2011**, *92*, 361–363. [[CrossRef](#)]
113. Toro, J.; Miller, E.L.; Prokopiev, A.V.; Zhang, X.; Veselovskiy, R. Mesozoic orogens of the Arctic from Novaya Zemlya to Alaska. *J. Geol. Soc.* **2016**, *173*, 989–1006. [[CrossRef](#)]
114. Embry, A. Geological and Geophysical Evidence in Support of the Hypothesis of Anticlockwise Rotation of Northern Alaska. *Mar. Geol.* **1990**, *93*, 317–329. [[CrossRef](#)]
115. Grantz, A.; Clark, D.L.; Phillips, R.L.; Srivastava, S.P.; Blome, C.D.; Gray, L.B.; Haga, H.; Mamet, B.L.; McIntyre, D.J.; McNeil, D.H.; et al. Phanerozoic stratigraphy of Northwind Ridge, magnetic anomalies in the Canada basin, and the geometry and timing of rifting in the Amerasia basin, Arctic Ocean. *Geol. Soc. Am. Bull.* **1998**, *110*, 801–820. [[CrossRef](#)]
116. Lawver, L.A.; Grantz, A.; Gahagan, L.M. Plate kinematic evolution of the present Arctic region since the Ordovician. In *Tectonic Evolution of the Bering Shelf–Chukchi Sea–Arctic Margin and Adjacent Landmasses. Special Paper*; Miller, E.L., Grantz, A., Klemperer, S.L., Eds.; The Geological Society of America: Boulder, CO, USA, 2002; Volume 360, pp. 333–358. [[CrossRef](#)]



© 2020 by the authors. Licensee MDPI, Basel, Switzerland. This article is an open access article distributed under the terms and conditions of the Creative Commons Attribution (CC BY) license (<http://creativecommons.org/licenses/by/4.0/>).